Geophysical Journal International

Geophys. J. Int. (2022) **228,** 1684–1712
Advance Access publication 2021 October 28
GJI Geodynamics and Tectonics

https://doi.org/10.1093/gji/ggab427

Links between foreland rheology and the growth and evolution of a young mountain belt in New Guinea

Lizzie Knight ,[1] Alex Copley ,[1] Claudia Bertoni ,[2] R. Alastair Sloan [3] and Richard Walker [2]

[1]*COMET, Bullard Laboratories, Department of Earth Sciences, University of Cambridge, Cambridge CB*2 3*EQ, UK. E-mail: epk26@cam.ac.uk*
[2]*Department of Earth Sciences, University of Oxford, Oxford OX*1 3*AN, UK*
[3]*Department of Geological Sciences, University of Cape Town, Cape Town* 7700*, South Africa*

Accepted 2021 October 18. Received 2021 October 15; in original form 2021 May 13

SUMMARY

We have studied the active and recent tectonics of New Guinea, using earthquake source modelling, analysis of gravity anomalies, seismic reflection profiles, and thermal and mechanical models. Our aim is to investigate the behaviour and evolution of a young continental deformation belt, and to explore the effects of lateral variations in foreland rheology on the deformation. We find that along-strike gradients in the lithosphere thickness of the southern foreland have resulted in correlated changes in seismogenic thickness, likely due to the effects on the temperature structure of the crust. The resulting variation in the strength of the foreland means that in the east, the foreland is broken through on thrust faults, whereas in the west it is relatively intact. The lack of correlation between the elevation of the mountain belt and the seismogenic thickness of the foreland is likely to be due to the time taken to thicken the crust in the mountains following changes in the rheology of the underthrusting foreland, as the thinned passive margin of northern Australia is consumed. The along-strike variation in whether the force exerted between the mountains and the lowlands is able to break the foreland crust enables us to estimate the effective coefficient of friction on foreland faults to be in the range of 0.01–0.28. We use force-balance calculations to show that the recent tectonic re-organization in western New Guinea is likely to be due to the development of increasing curvature in the Banda Arc, and that the impingement of continental material on the subduction zone may explain the unusually low force it exerts on western New Guinea.

Key words: Earthquake source observations; Seismicity and tectonics; Continental margins: convergent; Neotectonics; Rheology: crust and lithosphere; Rheology and friction of fault zones.

1 INTRODUCTION

The rheology of continental lithosphere—and its controls on tectonic deformation—has long been the source of debate. Discussion has surrounded the distribution of strength in continental lithosphere, and rheological differences between Precambrian cratons and younger intervening deformation belts (e.g. Chen & Molnar 1983; Maggi *et al.* 2000a; Townend & Zoback 2000; Burov & Watts 2006; Jackson *et al.* 2008; Burov 2010). One of the main methods that has been used to estimate the strength of the lithosphere is based upon observations and models of active mountain ranges and their forelands. The distribution of strain within the ranges can be used to estimate the material properties of the mountain belt, and flexure and earthquakes in the bounding forelands can be used to infer their rheology (e.g. Dalmayrac & Molnar 1981; England & Houseman 1989; England & Molnar 2015). However, most of this previous work has focused on relatively long-lived mountain belts like Tibet and the Andes, in which the foreland now adjacent to the ranges represents the former continental interior of the bounding plates. In order to fully explore the degree, and causes, of lateral variability in continental rheology, it is therefore important to investigate immature collision zones, where the foreland at least partially represents the continental margin of the bounding plate.

For this reason, we have chosen to study New Guinea, where the laterally variable continental margin of the northern Australian Plate forms the southern foreland to the deformation belt. This mountain range—the New Guinea Highlands—is the product of a young, active arc-continent collision, caused by rapid oblique convergence between the Australian and Pacific Plates (presently 110 mm yr^{-1}; DeMets *et al.* 1994). The orogeny is thought to have begun in the mid-Miocene (Hill & Hall 2003; Cloos *et al.* 2005), and the underthrusting Australian foreland displays large pre-existing structural variations along-strike. Thus New Guinea provides an ideal opportunity to study how along-strike variations in the mechanical properties and rheology of the lithosphere can affect the early stages of mountain-building.

In this paper, we use seismological modelling techniques to determine accurate source parameters for recent earthquakes in central and western New Guinea. We combine these data with elastic and thermal modelling to study along-strike rheological variation in the New Guinea Highlands and southern foreland basin. Using additional geodetic and seismic reflection data, we also explore the tectonic configuration and evolution of the region west of the mountains, where the deformation pattern has switched from regional compression to extension over the last 2 Myr. We make new estimates of the forces acting between the central mountains and forelands and estimate the frictional strength of active foreland faults. We suggest how along-strike variations in foreland lithospheric strength and mountain elevation may be related to each other, and explore the implications for the factors controlling the deformation in the early stages of mountain building. We also investigate how changing plate-driving forces in southeast Asia have controlled the tectonic evolution of western New Guinea through the late Cenozoic.

We begin by summarizing the geological history and current tectonic setting of the region. We then present newly constrained estimates of depths and focal mechanisms of earthquakes in New Guinea, before investigating lithosphere strength within the mountains and forelands. We then describe new evidence for recent and active extension in western New Guinea. We reconcile our observations with models of the lateral variations in the rheology of the lithosphere, and discuss how the New Guinea Highlands may be expected to evolve over time. Finally, we discuss how large-scale tectonic changes in the wider Indonesian region may have affected the tectonics of western New Guinea.

2 GEOLOGICAL HISTORY AND TECTONIC SETTING

2.1 Geology of New Guinea

New Guinea is situated on the northern edge of the Australian Plate. The island's geology reveals a complicated tectonic history of subduction, obduction, arc-continent collision, and mountain-building, driven by rapid oblique convergence between the Australian and Pacific plates.

New Guinea has been described as resembling a bird flying west (Moore 2003). The island is thus divided geographically into (from west to east): the Bird's Head, Neck, Body and Tail. Central New Guinea, or the Bird's Body, can itself be divided into three major WNW–ESE trending provinces (Fig. 1c): the Southern Lowlands, a stable platform which marks the northern extent of the Australian Plate; the New Guinea Highlands, formed primarily of passive margin sediments which have been folded and thrust to form mountains with an average elevation of 2–3 km; and the Mobile Belt, a northern accretionary complex of ophiolites, metamorphic rocks, sediments and island arc volcanics (Abers & McCaffrey 1988; Nash *et al.* 1993; Hill & Hall 2003; Baldwin *et al.* 2012).

The Southern Lowlands are comprised of Australian continental crust and form the foreland to the New Guinea Highlands. The Lowlands are divided by the Tasman Line (Fig. 1b), a boundary which separates Proterozoic cratonic basement of the Australian Shield in the west from the Palaeozoic Tasman Orogen in the east (Schiebner 1974; Hamilton 1979; Plumb 1979). The Tasman Line approximately follows the Indonesia–Papua New Guinea border, but its location north of the Lowlands is poorly known (Hill & Hall 2003). The Tasman Line is also roughly coincident with a change in lithosphere thickness observed in both New Guinea and Australia, such that the lithosphere is up to 100 km thicker to the west of the Tasman Line (Priestley *et al.* 2018, and discussed in more detail below).

In western New Guinea, the Bird's Head, Bird's Neck and Cenderawasih Bay comprise the Bird's Head Block, a region of Palaeozoic basement overlain and intruded by basin sediments, granitic intrusions, accreted arc material and high grade metamorphics (Pieters *et al.* 1983; Bailly *et al.* 2009; Jost *et al.* 2018). Eastern Papua New Guinea hosts the accreted Finisterre Arc (Davies *et al.* 1997; Hill & Raza 1999), and extensive ophiolite belts and arc magmatism along the Papuan Peninsula (Davies & Jaques 1984; Baldwin *et al.* 2012; Davies 2012).

2.2 Geological history

During the Palaeozoic, westwards subduction along the eastern margin of Australia (which was then part of Gondwana) led to terrane accretion above the subduction zone and the development of the Tasman Orogen, which was thrust westwards over the stable Precambrian craton which now forms western Australia and New Guinea (Crawford *et al.* 2003; Glen 2005). North–south rifting along the northern Australian margin in the Mesozoic lead to the truncation of the Tasman Orogen and the development of a passive margin up to 1000 km wide across what is now New Guinea (Pigram & Symonds 1991; Veevers *et al.* 1991; Cloos *et al.* 2005).

Major tectonic change occurred in the early Eocene after the breakup of Gondwana, when the Australian Plate drifted northwards as it separated from Antarctica (Royer & Sandwell 1989; Hall 2002). Pacific lithosphere was subducted beneath the north and east sides of the Australian passive margin, developing a volcanic island arc (Hill & Hall 2003). Around 30 Ma, the arrangement of the plate margins changed such that oceanic Australian lithosphere from the northern passive margin began subducting northwards beneath the volcanic arc (Cloos *et al.* 2005). Northwards subduction of the Australian Plate also occurred in the early Miocene beneath the Solomon Sea (Webb *et al.* 2014).

Subduction of the Australian Plate ceased between 15 and 12 Ma, when Australian continental crust reached the collision zone, and crustal shortening and orogenesis was initiated across central New Guinea (Visser & Hermes 1962; Pigram *et al.* 1989; Pigram & Symonds 1991; Cloos *et al.* 2005; Webb *et al.* 2014). The New Guinea Highlands were formed primarily of deformed sediments from the passive margin and accretionary prism. North of the orogeny, the Mobile Belt was developed as terranes from the volcanic arc and forearc basin, containing ophiolites, metamorphic rocks, intrusives and sediments, were accreted to the northern Australian margin (Hamilton 1979; Nash *et al.* 1993; Davies *et al.* 1997). The mid-Miocene also saw the active Java subduction zone propagate eastwards through Indonesia and begin to subduct an embayment of Indian oceanic crust from the western edge of Australian continent, initiating subduction along the Banda Arc (Spakman & Hall 2010, Fig. 1b).

In the late Miocene, Pacific lithosphere began to subduct southwards beneath the north coast of New Guinea (Tregoning & Gorbatov 2004). Orogenic deformation and sedimentary deposition

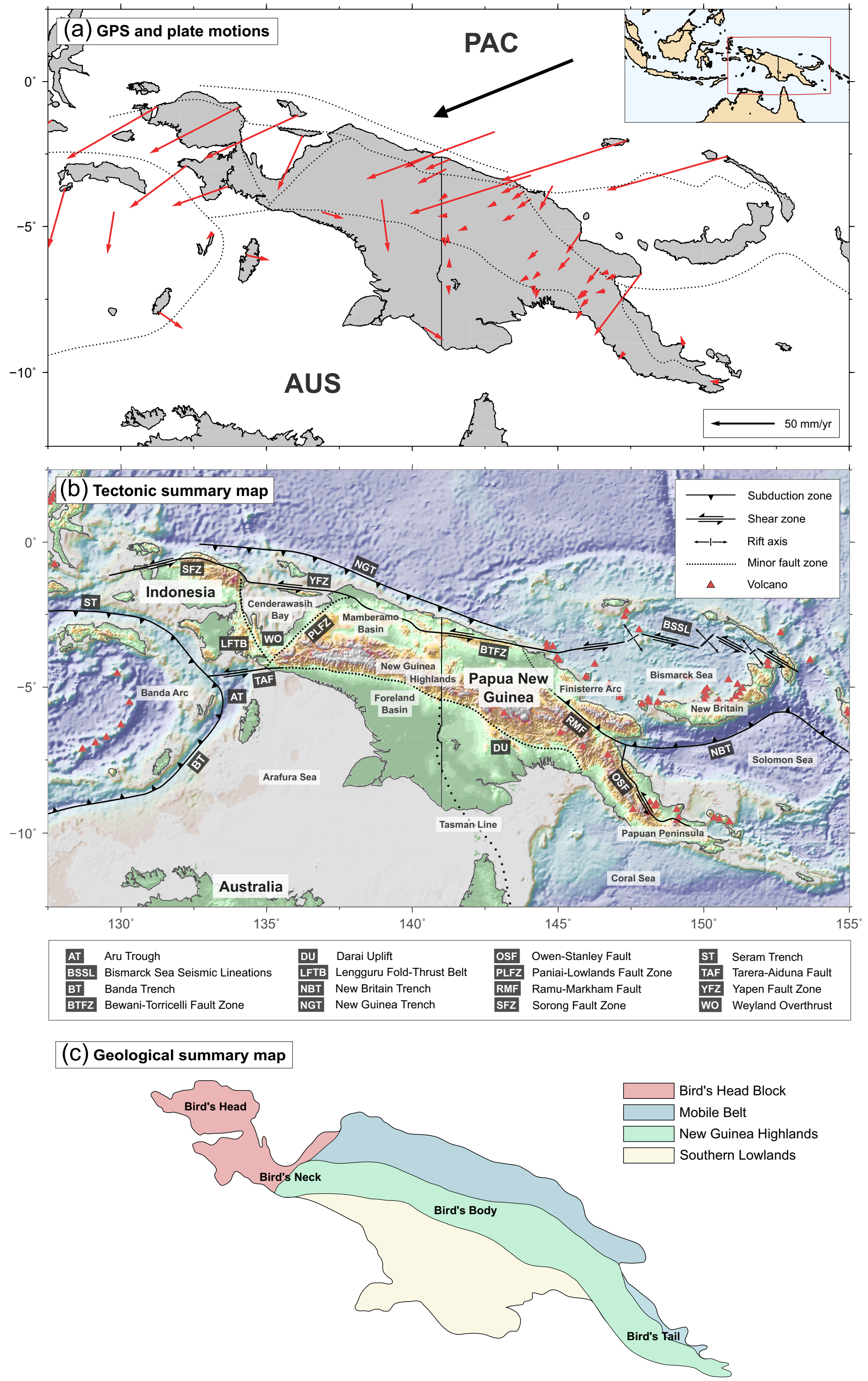

Figure 1. (a) GPS data (red arrows) showing motion relative to Australian Plate (AUS). GPS data west of 141°E are from Stevens *et al.* (2002); GPS data east of 141°E are from Koulali *et al.* (2015). The large black arrow indicates motion of the Pacific Plate (PAC) relative to the Australian Plate (DeMets *et al.* 1994). Dotted lines indicate key fault zones adapted from Baldwin *et al.* (2012). (b) Tectonic summary map of New Guinea showing major geological features and fault zones, adapted from Baldwin *et al.* (2012). Red triangles indicate locations of known volcanoes (Siebert *et al.* 2011). Acronyms of the names of fault zones are listed below the map. (c) Simplified geological map of New Guinea adapted from Hill & Hall (2003) and Baldwin *et al.* (2012).

propagated rapidly southwards from the Mobile Belt into the southern fold-and-thrust belt (Pigram & Symonds 1991; Hill & Raza 1999). Trench-parallel strike-slip activity occurred along shear zones in western and central New Guinea (Dow & Sukamto 1984; Cloos *et al.* 2005; Bailly *et al.* 2009), whilst shortening remained dominant in the east (Hill & Hall 2003).

In the late Miocene and Pliocene, northwards subduction of oceanic lithosphere in Cenderawasih Bay led to collision between the Bird's Neck and the Weyland Overthrust, which formed the Lengguru Fold-Thrust Belt (Dow & Sukamto 1984; Hill & Hall 2003; François *et al.* 2016; Fig. 1b). From the Pliocene onwards, compression waned across the central New Guinea Highlands, as strike-slip tectonics became dominant at high elevation and thrusting migrated to the presently-active thrust front on the southern edge of the range (Abers & McCaffrey 1988; Cloos *et al.* 2005). Pliocene and Quaternary volcanism has been identified within the Highlands, though its origin is debated (e.g. Johnson *et al.* 1978; Hamilton *et al.* 1983; McDowell *et al.* 1996; Cloos *et al.* 2005). The most recent major tectonic change occurred around 2 Ma when the Bird's Neck and Cenderawasih Bay became a region of transtension, with deformation taken up along the edges of the bay and the Tarera-Aiduna Fault (Pubellier & Ego 2002; Bailly *et al.* 2009).

2.3 Present tectonic setting

At present, the broad-scale tectonics of central New Guinea are driven by oblique convergence between the Australian and Pacific plates, which occurs at a rate of 110 mm yr^{-1} along an azimuth of 248° (DeMets *et al.* 1994, Fig. 1a). The convergence is oblique to the trend of major geological structures in central New Guinea (Fig. 1b) and has been partitioned into ∼70 mm yr^{-1} of shortening and ∼85 mm yr^{-1} of left-lateral shear across these structures (Dow & Sukamto 1984; Abers & McCaffrey 1988; Puntodewo *et al.* 1994; McCaffrey 1996; Tregoning & Gorbatov 2004). GPS and seismic data suggest that between 10 and 60 mm yr^{-1} of the shortening may be accommodated by subduction off the north coast at the New Guinea Trench, which produces occasional megathrust earthquakes such as the M_w 8.2 earthquake on 2 February 1996 (McCaffrey 1996; Stevens *et al.* 2002; Tregoning & Gorbatov 2004). The remaining shortening across the central part of the island is taken up on thrust faults within the New Guinea Highlands and Mamberamo Basin (McCaffrey & Abers 1988; Puntodewo *et al.* 1994; Wallace *et al.* 2004).

Central and western New Guinea is dominated by left-lateral strike-slip tectonics. Along the north coast of the island, a semi-continuous shear zone runs subparallel to the New Guinea Trench. From west to east, this shear zone is divided into the Sorong, Yapen and Bewani-Torricelli Fault Zones (Fig. 1b). The shear zone exhibits a varying slip rate along-strike: GPS data reveal the Yapen Fault Zone to be slipping at up to 46 mm yr^{-1} (Bock *et al.* 2003), while the Sorong Fault Zone may slip at ∼20 mm yr^{-1} west of 131°E but is mostly inactive where it outcrops on land (Puntodewo *et al.* 1994; Stevens *et al.* 2002). Accumulated offset along the Sorong and Yapen Fault Zones is estimated between 370 and 900 km (Visser & Hermes 1962; Dow & Sukamto 1984; Charlton 1996). The Tarera-Aiduna Fault, which lies south of Cenderawasih Bay and the Lengguru Fold-Thrust Belt (Fig. 1b), has an estimated left-lateral offset of 50 km (Hamilton *et al.* 1983) and a slip rate of 20 mm yr^{-1} (McCaffrey & Abers 1991). The Tarera-Aiduna Fault continues offshore to the west where it meets the Seram Trench (Teas *et al.* 2009). Some left-lateral strain is also taken up along the Paniai-Lowlands Fault Zone, which truncates the New Guinea Highlands on the east side of Cenderawasih Bay. Faults within the Paniai-Lowlands Fault Zone display up to 1.5 km of vertical offset (Pubellier & Ego 2002) and may accommodate ∼20 mm yr^{-1} of extension (Stevens *et al.* 2002), which suggests a transtensional nature to the fault zone.

Off the west coast of New Guinea, the Banda Arc represents an active collision between the Australian continental margin and a volcanic arc (Carter *et al.* 1976; Hamilton 1979; McCaffrey & Abers 1991). Australian continental crust is being underthrust both northwards at the Banda Trench and southwestwards at the Seram Trench, where the Bird's Head Block meets the arc (Fig. 1b). Deep seismicity implies that this continental material is connected to subducting oceanic lithosphere at depth (McCaffrey 1989). The tight curvature of the arc has sparked debate regarding whether the collision involves deformation of a single continental slab at both trenches (Hamilton 1979; Spakman & Hall 2010), or two separate slabs subducting towards each other (Cardwell & Isacks 1978; McCaffrey 1989; Hinschberger *et al.* 2005).

In eastern Papua New Guinea, an active arc-continent collision is emplacing the Finisterre Arc onto the northeast coast of the island along the Ramu-Markham Fault (Fig. 1b), with maximum convergence rates between 40 and 60 mm yr^{-1} (Davies *et al.* 1997; Wallace *et al.* 2004; Koulali *et al.* 2015). Convergence continues along-strike at the New Britain Trench. The Owen-Stanley Fault Zone on the Papuan Peninsula shows along-strike tectonic variability, transitioning from extension at the southern tip, to oblique-sinistral slip which is exhuming a metamorphic core complex, to shortening in the north where the fault zone meets the Ramu-Markham Fault (Wallace *et al.* 2004; Daczko *et al.* 2011).

Within this overall context, we have chosen to study the active tectonics of the New Guinea Highlands and southern foreland basin, as well as investigating active extension in the Bird's Neck and Cenderawasih Bay. We will first describe new estimates of earthquake depths and mechanisms in both regions, which we have made in order to study how variation in lithosphere properties may be affecting the active tectonics. Our seismological methods are detailed in the following section.

3 SEISMICITY

3.1 Earthquake source parameter modelling

To study active deformation in central and western New Guinea, we have compiled a set of earthquakes which have been modelled to determine their source parameters, and have added to them 23 of our own analyses. Focal mechanisms and centroid depths determined by teleseismic body-waveform modelling were taken from the work of Abers & McCaffrey (1988) and Sloan & Jackson (2012). Of the new events analysed in this study, 14 events were studied using body-waveform modelling to determine depth, focal mechanism, magnitude and source time function (Table 1), and nine events were modelled using depth-phase analysis to estimate depth alone (Table 2). We chose to model these earthquakes in order to study the range of faulting styles in the southern foreland basin, New Guinea Highlands and the Bird's Neck. While estimates of earthquake source parameters are available in online catalogues such as the gCMT (Dziewonski *et al.* 1981; Ekström *et al.* 2012) or ISC-EHB Bulletin (Weston *et al.* 2018; International Seismological Centre 2021), the methods used in our study can significantly increase the accuracy of the source parameter estimates, in particular the centroid depth (Engdahl *et al.* 2006).

Table 1. Earthquake source parameters determined in this study using body-waveform modelling. Depths and focal mechanisms have been determined using the MT5 program, except for the events marked † for which focal mechanisms could not be accurately obtained. For these two events, the gCMT focal mechanism has been retained (Dziewonski *et al.* 1981; Ekström *et al.* 2012), and only depth, source time function and seismic moment inverted for.

Body-waveform modelling												
	Date			Time		Long	Lat	M_w	Depth	Focal mechanism		
yyyy	mm	dd	hh	mm	ss	(°)	(°)		(km)	Strike (°)	Dip (°)	Rake (°)
1992	05	25	02	51	32	139.73	−4.79	5.7	6	303	66	22
1993	06	12	18	26	42	135.12	−4.38	6	10	251	72	19
1994	01	04	19	31	59	135.15	−4.30	6	8	69	86	350
1995	03	13	10	31	46	134.38	−2.79	5.8	7	208	58	272
2000	03	03	22	22	40	143.81	−6.82	6.6	18	122	52	82
†2005	02	02	06	28	36	145.04	−7.48	5.5	14	63	59	68
2007	08	20	21	30	45	140.87	−5.40	5.7	11	149	34	91
2011	11	15	23	42	29	140.31	−5.28	5.7	14	126	48	52
2012	10	12	00	31	28	134.03	−4.89	6.6	23	183	54	243
2012	12	08	16	35	16	143.97	−7.21	5.8	9	133	54	99
†2013	09	05	15	27	03	144.03	−7.27	5.4	5	112	54	85
2014	07	28	23	0	48	143.87	−6.92	5.6	13	131	44	100
2018	03	06	14	13	07	142.61	−6.30	6.7	10	135	75	93
2019	01	26	08	12	48	133.77	−5.50	5.9	30	204	58	253

Table 2. Earthquake depths determined using depth-phase analysis in this study. Focal mechanisms and moment have been retained from the gCMT catalogue (Dziewonski *et al.* 1981; Ekström *et al.* 2012).

Depth-phase analysis												
	Date			Time		Long	Lat	M_w	Depth	gCMT mechanism		
yyyy	mm	dd	hh	mm	ss	(°)	(°)		(km)	Strike (°)	Dip (°)	Rake (°)
1991	02	23	19	53	16	137.71	−4.68	5.2	6	108	64	99
1995	01	21	16	44	07	134.35	−2.60	5.2	7	214	58	292
1999	10	25	00	43	06	134.19	−2.12	5.4	8	31	38	267
2001	07	12	19	37	15	134.84	−3.65	5.1	8	191	60	251
2002	09	28	15	14	57	134.57	−3.26	5	10	26	55	283
2007	08	19	19	09	45	140.85	−5.37	5.3	9	80	87	3
2009	10	29	01	34	00	140.38	−5.26	5.1	19	140	43	101
2016	06	14	22	09	28	137.97	−4.60	5.2	33	296	68	129
2019	04	27	13	32	53	137.23	−4.32	4.9	8	235	26	293

Teleseismic body-waveform modelling can be used for earthquakes of sufficient magnitude to result in good signal-to-noise ratio at teleseismic distances (typically $M_w \geq 5.4$) and with good azimuthal seismic station coverage. In this study, earthquake source parameters were determined using the MT5 program, which performs a joint inversion of *P* and SH seismic waveforms recorded at teleseismic distances (McCaffrey & Abers 1988; McCaffrey *et al.* 1991; Zwick *et al.* 1994). The methodology behind this procedure has been extensively detailed in previous literature (e.g., Abers & McCaffrey 1988; Molnar & Lyon-Caen 1989; Taymaz *et al.* 1990) and need only be summarized here.

Broadband seismograms were downloaded from the IRIS DMC and deconvolved to reproduce the response of a long-period (15–100 s) WWSSN instrument. This process allows the earthquake to be modelled as a point source and reduces sensitivity to small-scale heterogeneities in velocity structure in the source region (Taymaz *et al.* 1990). For earthquakes within the foreland basin and Bird's Neck, we use a simple two-layer velocity model which represents an upper layer of sediments (V_p = 4.5 km s^{-1}; V_s = 2.7 km s^{-1}; density = 2400 kg m^{-3}; layer thickness = 2 km) and a crustal layer which hosts the earthquake source (V_p = 6.5 km s^{-1}; V_s = 3.8 km s^{-1}; density = 2800 kg m^{-3}). Reasonable changes to the velocity structure alter the earthquake source depth only within the limits of expected uncertainties (±4 km; Taymaz *et al.* 1990) and so the thickness of the upper sediment layer was not altered for each individual event. For events in the Aru Trough, we use a water layer with a thickness of 3.0–3.5 km (adjusted to match the observed water layer reverberations), a sediment layer (V_p = 3.0 km s^{-1}; V_s = 1.7 km s^{-1}; density = 2400 kg m^{-3}; layer thickness = 5 km) and a lower crustal layer (V_p = 6.5 km s^{-1}; V_s = 3.8 km s^{-1}; density = 2800 kg m^{-3}) (Jacobson *et al.* 1979; Sloan & Jackson 2012).

Seismic stations within 30–90° epicentral distance of the earthquake were selected in order to avoid lithospheric reverberations and interactions with the core. Up to 50 P and SH seismograms were selected after visual inspection of signal-to-noise ratio and to ensure sufficient azimuthal coverage. The gCMT solution was then used as the starting model for the inversion, which minimizes the weighted least-squares misfit between the observed seismograms and synthetic seismograms generated from the starting model. Seismograms were weighted by azimuthal density, and *P* phases weighted by a factor of two compared to SH phases, to account for their lower amplitude. The final solution was constrained to have a double-couple moment tensor. An example focal mechanism produced using this method for the 15 November 2011 M_w 5.7 earthquake in the New Guinea foreland is shown in Fig. 2. The parameters of all earthquakes with new analyses performed in this study are given in Table 1, and our inversion results for all events are displayed in the supplemental information.

Uncertainties in the source parameters were estimated using the method of Taymaz *et al.* (1990). Each source parameter was

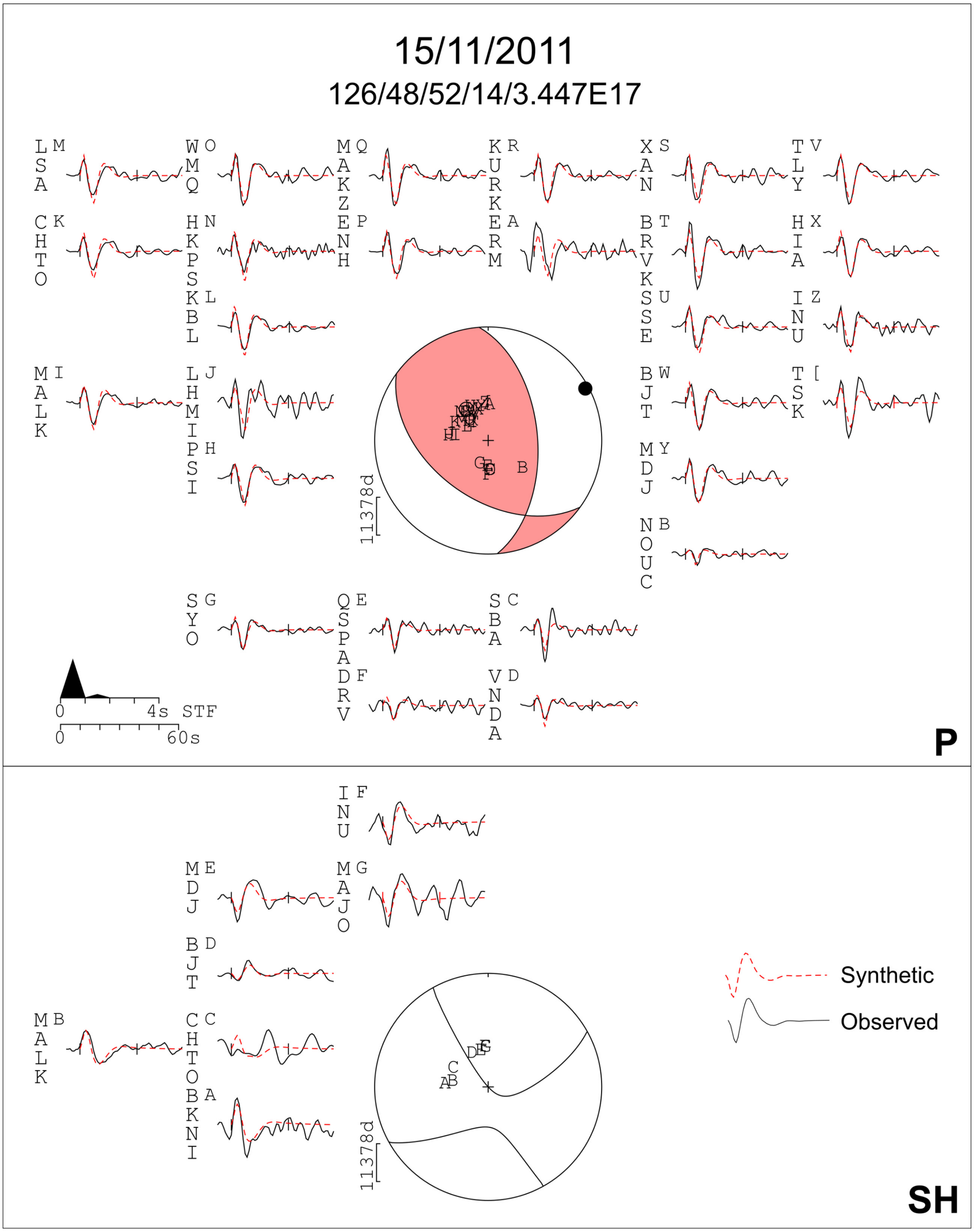

Figure 2. Minimum-misfit focal mechanism solution for the 15 November 2011 M_w 5.7 earthquake in the New Guinea forelands, determined using teleseismic body-waveform modelling in the MT5 program. Source parameters from the inversion are shown beneath the title in the form: strike/dip/rake/centroid depth/seismic moment, where centroid depth is in kilometres and seismic moment is in Newton metres. The upper panel shows the lower-hemisphere stereographic projection of the *P*-waveform nodal planes and the locations of seismic stations used in the inversion. The lower panel shows the SH-waveform equivalent. Letters printed on the focal spheres correspond to letters next to the seismic station codes, ordered by azimuthal location. Seismic station codes are printed to the left of each seismogram. Black and white circles on the focal spheres represent the projections of the *P*- and *T*-axes, respectively. The black lines and dashed red lines represent the observed and synthetic seismograms, respectively. Vertical ticks on each seismogram mark the inversion window. STF represents the best-fitting source–time function, with the timescale for the inverted waveforms shown directly below.

successively fixed and an inversion performed in which all other source parameters were free to vary. The fixed parameter was varied sequentially on either side of the minimum misfit value. The potential error was estimated by examining when the fit to the observed waveforms was noticeably degraded. Errors in centroid depth were typically within ±5 km. Errors in focal mechanism were more variable and highly dependent on the azimuthal distribution of seismic stations: strike errors were typically within ±30°; dip errors within ±15° and rake errors within ±30°. For the 2 February 2005 M_w 5.5 earthquake and the 5 September 2013 M_w 5.4 earthquake, the depth was well constrained by the MT5 program but the focal mechanism was not, primarily due to poor seismic station coverage of the focal sphere. For these two events, the gCMT focal mechanism solution was retained and we inverted only for centroid depth, magnitude, and source time function.

For earthquakes of M_w <5.5, or if azimuthal coverage was poor, or if there were few seismic stations with an acceptable signal-to-noise ratio to allow inversion for the focal mechanism, forward-modelling of depth phases was instead used to constrain the source depth of the event. This method compares the *P* wave and pP and sP near-source surface reflections between an observed seismogram and a synthetic seismogram generated for a range of source depths, in order to find the best-fitting depth. For each earthquake, broadband seismograms with visible depth phases were selected, within the 30–90° epicentral range. Synthetic seismograms were generated using the WKBJ algorithm (Chapman *et al.* 1988), the ak135 global velocity model (Kennett *et al.* 1995), and the gCMT focal mechanism (Dziewonski *et al.* 1981; Ekström *et al.* 2012). The observed *P* waves were aligned with the first arrival of their corresponding synthetic. The absolute amplitude of the synthetic was scaled to fit the amplitude of the observed seismogram. By varying the source depth used to calculate the synthetic waveforms, the best-fitting solution was selected via visual inspection of the synthetic and observed depth phases. Errors in source depth were typically ±1 km.

For events we were unable to model ourselves due to limited data availability or quality, we have used additional data from the gCMT catalogue and ISC-EHB Bulletin (Dziewonski *et al.* 1981; Ekström *et al.* 2012; Weston *et al.* 2018; International Seismological Centre 2021). A merged earthquake catalogue was created, using gCMT focal mechanism solutions matched to events located by the ISC-EHB Bulletin; this was done because locations and depths located using the EHB algorithm are typically more accurate than those from the gCMT catalogue (Engdahl *et al.* 1998, 2006). The merged catalogue contains more than 4700 events of M_w >4.5 which occurred between 1976 and 2016 across New Guinea.

3.2 Patterns of seismicity

The focal mechanisms of earthquakes modelled in this study and by Abers & McCaffrey (1988) and Sloan & Jackson (2012) are displayed in Fig. 3, alongside the additional events from the gCMT catalogue. Fig. 4 shows the location and depths of earthquakes across New Guinea, separated by focal mechanism.

The north coast of New Guinea is dominated by shallow, left-lateral strike-slip earthquakes which are likely to be associated with the semi-continuous Sorong, Yapen and Bewani-Torricelli Fault Zones, and reverse-faulting earthquakes associated with the New Guinea Trench; these reverse earthquakes generally have much greater magnitudes than the strike-slip events. There is also some strike-slip and reverse-faulting activity within the Mamberamo Basin.

Seismicity in northeast New Guinea is dominated by a major north-dipping subduction zone (the New Britain Arc) which runs from the northeast of the island offshore towards the island of New Britain. Deep earthquakes (>60 km) beneath the northeast New Guinea Highlands may be related to subduction along this arc. The strike-slip earthquakes concentrated along the northern coastline extend from the Bewani-Torricelli Fault Zone to the region north of the Bismarck Sea.

The overall pattern of seismicity in and around the New Guinea Highlands shows only a small amount of shallow crustal deformation presently occurring beneath the mountains (Figs 3 and 4). The largest earthquakes in the region are strike-slip events, indicating that there is little active crustal shortening within the range. The largest magnitude earthquakes are concentrated beneath the western half of the Highlands. Earthquakes beneath the Highlands at depths greater than ∼60 km are likely associated with southwards subduction of the Pacific Plate at the New Guinea Trench, instead of being associated with the orogeny. The southern range-front of the Highlands is characterized by thrust-faulting earthquakes with nodal planes aligned approximately parallel to the strike of the range front. These events tend to have nodal planes with dips >30°. Our modelling techniques do not allow us to constrain which of the nodal planes is the fault plane, though for these thrust-faulting events the fault plane is likely to be the north-dipping plane, causing uplift in the fold-thrust belt and subsidence in the basin. South of the foreland basin, the Southern Lowlands are mostly aseismic, with the exception of a small number of events that we discuss in detail later.

To the west of the New Guinea Highlands, significant seismicity occurs within the Bird's Neck and along the edges of Cenderawasih Bay. Where the Highlands meet the Bird's Neck, the region is dominated by shallow strike-slip earthquakes, some of which are likely associated with the Tarera-Aiduna Fault which continues westwards towards the Banda Arc. To the south of the Bird's Neck, normal and strike-slip faulting is observed within the Aru Trough. The east side and north sides of Cenderawasih Bay show mostly strike-slip earthquakes, whereas the west side is characterized by shallow normal faulting. Seismic activity in the Bird's Head is concentrated along the north coast and is associated with the Sorong Fault Zone and the New Guinea Trench.

4 NEW GUINEA HIGHLANDS AND FORELANDS

We now examine in detail the New Guinea Highlands and their southern foreland, and combine our estimated earthquake source parameters with thermal models and the analysis of gravity anomalies.

4.1 Earthquake depths and seismogenic thickness

Earthquake depths in the New Guinea Highlands and southern foreland basin, determined by body-waveform modelling and depth-phase analysis, are shown in Fig. 5, overlain on a map of lithosphere thickness derived from surface wave tomography (Priestley *et al.* 2018). The vertical resolution of the lithosphere thickness data is approximately 30 km, and the horizontal resolution is between 250 and 400 km (Priestley *et al.* 2018). The deepest earthquakes (the 14 June 2016 M_w 5.2 event at 33 km depth in the foreland and the 2 December 1982 M_w 5.5 event at 44 km depth in the Highlands) occurred in the region of thickest lithosphere in New Guinea. The 1982 event also occurred in the region where mountain elevation is highest.

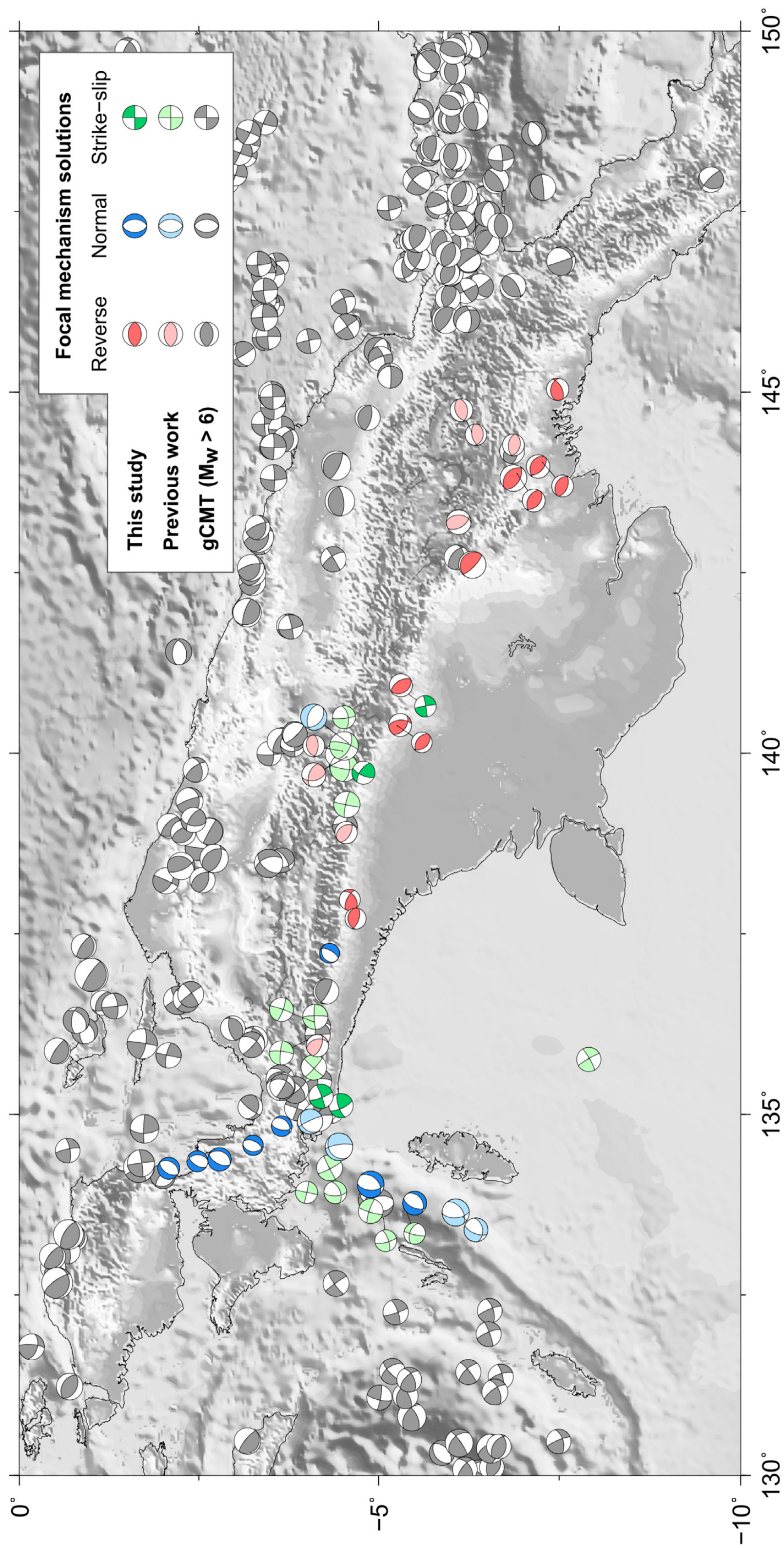

Figure 3. Focal mechanism solutions determined by body-waveform modelling or depth-phase analysis in this study, or by body-waveform modelling in previous work (Abers & McCaffrey 1988; Sloan & Jackson 2012). Additional events of M_w >6 are taken from the gCMT catalogue (Dziewonski *et al.* 1981; Ekström *et al.* 2012).

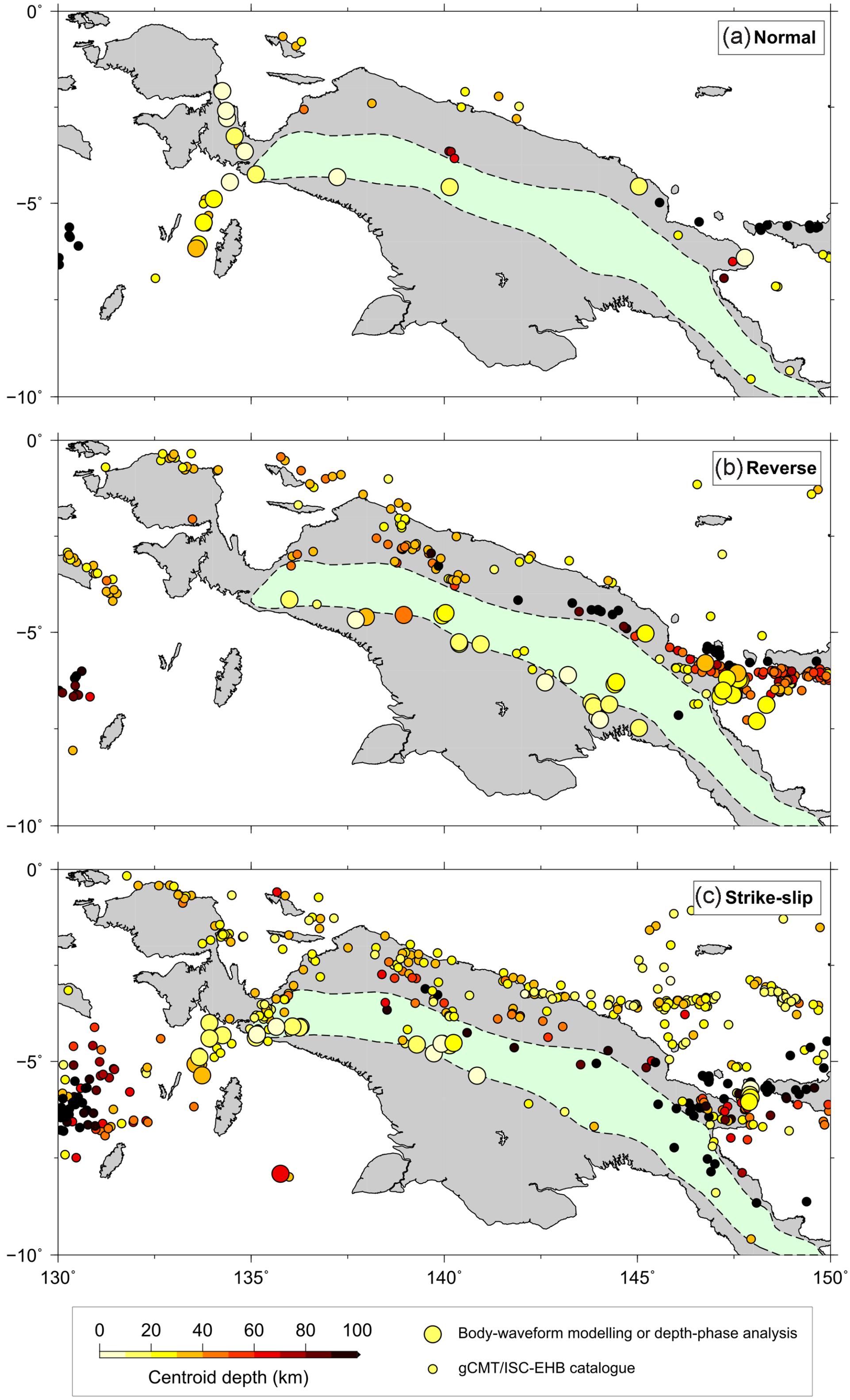

Figure 4. Maps of earthquake locations and depths, separated by focal mechanism. Large circles represent results from body-waveform modelling or depth-phase analysis in this study and previous work (Abers & McCaffrey 1988; McCaffrey & Abers 1991; Sloan & Jackson 2012). Additional events of $M_w \geq 5.5$ are shown as small circles and are taken from a catalogue of gCMT focal mechanism solutions combined with depths from the ISC-EHB Bulletin (Dziewonski *et al.* 1981; Ekström *et al.* 2012; International Seismological Centre 2021). The green outline marks the extent of the New Guinea Highlands.

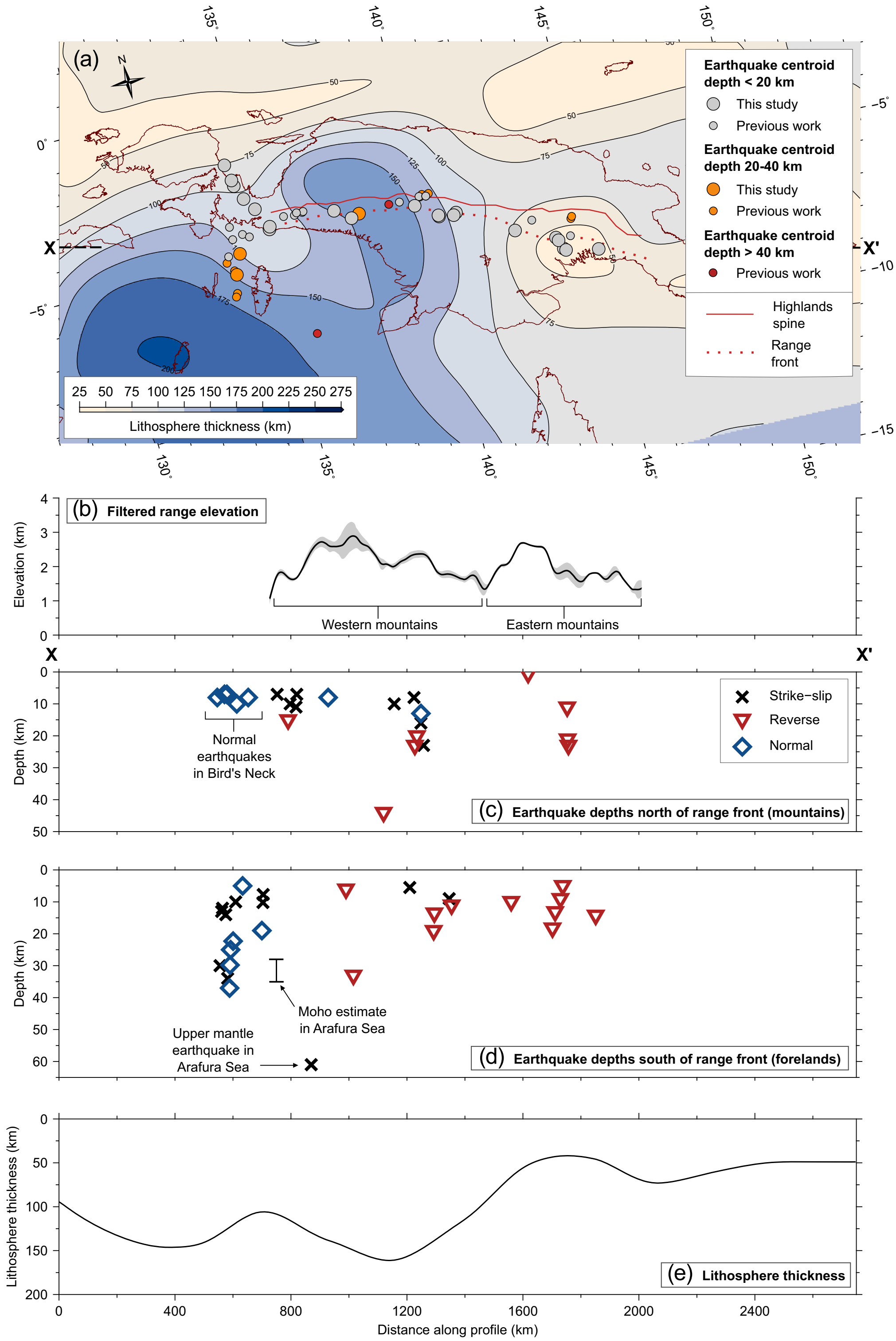

Figure 5. (a) Earthquake depths determined by body-waveform modelling or depth-phase analysis in this study or by previous work (Abers & McCaffrey 1988; Sloan & Jackson 2012), shown on a map of lithosphere thickness (Priestley *et al.* 2018). The lower bound on horizontal resolution of the lithosphere thickness data is ~250 km, and the vertical resolution is ~30 km. The lithosphere thickness data were defined on a 2-degree grid and have been interpolated to show a smoothed data set. Earthquakes are coloured according to centroid depth. X and X' represent the end points of the cross-section used in the lower panels. The solid red line represents the topographic spine of the New Guinea Highlands and the dotted red line represents the range front. (b) Topography of the New Guinea Highlands was taken from a 50 km swath along the spine of the New Guinea Highlands, from a 100 km Gaussian filtered version of the ETOPO2 data set. The black line represents mean elevation and the grey outline represents the standard deviation. (c and d) Centroid depths of earthquakes from panel (a) have been projected onto a vertical cross-section along-strike of the mountains, separated by whether the earthquake occurs north of the range front (within the mountains) or south of the range front (within the foreland basin or Arafura Sea). Estimates of Moho depth from the Arafura Sea (Jacobson *et al.* 1979) are taken to represent the crustal thickness of the northern Australian Shield. (e) Lithosphere thickness plotted along the cross-section X–X'.

We have used the modelled source depths of earthquakes to estimate the seismogenic thickness (T_s) of the lithosphere: namely, the thickness of the brittle part of the lithosphere which ruptures in earthquakes. For the magnitudes of the events we have studied (M_w 4.9–6.7), and for commonly observed displacement/length ratios (i.e. 5×10^{-5}, Scholz 1982), the rupture radius will be approximately between 2–16 km. When combined with the fault dips determined in our inversion analysis, the range of depth extents of the rupture patch are similar to, or smaller than, the depth uncertainties from our inversion methods, and are small compared with the variations we describe below. The earthquakes used to calculate seismogenic thickness in the foreland may not fully represent the seismicity of the region, due to our limited observation time compared with the duration of earthquake cycles. However, we have chosen not to supplement our data with earthquakes from the gCMT or ISC-EHB catalogues (Dziewonski *et al.* 1981; Ekström *et al.* 2012; International Seismological Centre 2021) as these catalogues provide less accurate depth estimates than body-waveform modelling or depth-phase analysis (Engdahl *et al.* 2006). As such, our estimates represent the minimum possible seismogenic thickness, given that future earthquakes may occur at greater depths. However, we are encouraged in our approach by previous studies that have established lateral variations in seismogenic thickness using similar numbers of earthquakes, which have been confirmed by microseismic surveys and not contradicted by subsequent events (Chen & Molnar 1983, 1990; Kayal & Zhao 1998; Maggi *et al.* 2000b; Priestley *et al.* 2008; Craig *et al.* 2011; Nissen *et al.* 2011; Sloan *et al.* 2011; Devlin *et al.* 2012; Nemati *et al.* 2013; Craig & Jackson 2021).

In the western foreland basin between 135°E and 141°E, the seismogenic thickness is 33–36 km. This estimate incorporates possible errors from our depth estimations, and uses the magnitudes of the earthquakes to estimate a maximum possible depth of rupture from our estimated centroid depths and magnitudes using a displacement/length ratio of 5×10^{-5} (Scholz 1982; Fig. 5c). We note that the earthquake depths determined using depth-phase analysis represent hypocentres instead of centroid depths, but the magnitude of these earthquakes is small (M_w<5.5) and so the maximum rupture depth is probably <3–4 km greater than the hypocentre depth. The seismogenic thickness in this western region is consistent with the depths of earthquakes near the Aru Trough on the western margin of the foreland (Sloan & Jackson 2012; blue diamonds on Fig. 5d). Given that receiver function studies have estimated the crustal thickness of the northern Australian shield, away from the edge of the plate, to be approximately 27–35 km (Jacobson *et al.* 1979; Clitheroe *et al.* 2000), our estimate of seismogenic thickness implies that the entire crust of the western foreland is seismogenic. Sloan & Jackson (2012) also identified two earthquakes in the Arafura Sea which occurred in the seismogenic upper mantle. The deepest earthquake in the New Guinea foreland (at 33 km) occurs within error of the Moho depth, however it is likely the Moho depth in the foreland is depressed compared to where it was measured in the Arafura Sea, due to the Australian plate bending as it underthrusts the mountains. Therefore it is more likely this earthquake occurred within the lower crust than in the upper mantle. In the eastern foreland basin between 141°E and 146°E, the seismogenic thickness is resolvably thinner, and is 20–27 km.

It is more difficult to estimate the seismogenic thickness within the New Guinea Highlands as we must differentiate between the earthquakes occurring within the seismogenic part of the over-riding plate, those within the underthrusting Australian plate, and those linked with south-dipping subduction at the New Guinea Trench. As the earthquake depths listed in the gCMT or ISC-EHB Bulletin catalogues are less accurate than depths estimated using body-waveform modelling (Engdahl *et al.* 2006), we have chosen to estimate the seismogenic thickness of the Highlands using only the body-waveform modelled solutions from Abers & McCaffrey (1988). If we consider all modelled events, T_s is between 46 and 48 km in the western Highlands (135–141°E) and between 24 and 26 km in the eastern Highlands (141–146°E). The crustal thickness of the Highlands is not well known, but is estimated to be ∼45 km (Abers & McCaffrey 1988; Abers & Lyon-Caen 1990), so it is possible that the seismogenic thickness represents a single crustal layer. However, the earthquakes are not distributed evenly through the crust in the western Highlands. Fig. 5(c) shows that almost all earthquakes beneath the western Highlands occur at depths shallower than 25 km. The deepest event, the reverse-faulting earthquake at 44 km and close to the range front, may represent an earthquake in the underthrusting plate, whilst the shallower earthquakes represent the seismogenic thickness of the upper plate. If this is the case, then the seismogenic thickness of the over-riding material is similar between the western and eastern Highlands.

4.2 Thermal modelling

Changes in seismogenic thickness along-strike of the southern foreland basin correlate with changes in lithosphere thickness (Fig. 5a; Priestley *et al.* 2018). In this section, we use thermal models to examine whether the along-strike variation in seismogenic thickness could be the result of along-strike variations in the thermal structure, due to the lithosphere thickness contrasts, or whether it implies variations in crustal composition. We have constructed simple steady-state geotherms for a range of values of lithosphere thickness and radiogenic heating in the crust. We use a wide range of values for lithosphere thickness to account for the broad horizontal resolution of the data (250–400 km). However, the east-west transition in lithosphere thickness is a major feature which stretches southwards into Australia, so we are confident that the data reflect a true gradient in lithosphere thickness along-strike of the basin.

In our thermal modelling, we have followed the methods of McKenzie *et al.* (2005), Copley *et al.* (2009) and Craig *et al.* (2020). The 1-D diffusion equation has been discretized and solved using a Crank–Nicholson (joint implicit-explicit) finite difference scheme (Press *et al.* 1992). The upper surface of each geotherm was held at 0 °C and the base of the lithosphere fixed at the isentropic temperature for that depth, calculated using a mantle potential temperature of 1315 °C. We follow the approach of Copley *et al.* (2009) and Craig *et al.* (2020) in approximating the thermal boundary layer at the boundary between the lithosphere and the convecting mantle as the isentropic temperature applied at that depth, which has minimal influence on the overlying thermal structure. We use temperature-dependent values of thermal conductivity and heat capacity (Hofmeister 1999; McKenzie *et al.* 2005; Whittington *et al.* 2009), incorporating granodiorite values for the crust (Miao *et al.* 2014) and olivine values for the mantle (McKenzie *et al.* 2005). Steady-state geotherms are calculated by inputting an initial (arbitrary) thermal structure (in this case a linear gradient from the surface to the base of the lithosphere), and allowing diffusion to occur until the evolution through time is insignificant. The time taken depends on the lithosphere thickness, which controls the thermal time constant of the lithosphere, and is <1 Gyr. At each time-step, we iterate multiple times, updating the temperature-dependent thermal parameters with each iteration. Such a measure is necessary because our finite difference scheme is centred in time, so the thermal parameters at the end of the time-step play a role in the computation (Press *et al.* 1992). We therefore maintain self-consistent temperatures and thermal parameters at each time-step.

Crustal thickness was held constant at 30 km (Jacobson *et al.* 1979; Clitheroe *et al.* 2000), and radiogenic heating assumed to be constant throughout the crust, based upon recent results suggesting that partial melting has a limited effect on the rate of radiogenic heating in the partitioned melt and residue, due to the growth and/or retention of relatively high-Th accessory minerals in the residue compensating for the removal of other heat-producing elements during partial melting and melt migration (Yakymchuk & Brown 2019; Weller *et al.* 2020). This assumption is consistent with the lack of observed correlation between metamorphic grade and rate of radiogenic heating in global compilations (Hasterok *et al.* 2018). Radiogenic heating in the mantle was assumed to be zero, as model geotherms calculated with no mantle radiogenic heating correlate well with *P*–*T* estimates from mantle xenoliths (e.g. Rudnick *et al.* 1998).

Fig. 6(a) shows a collection of our calculated geotherms for which lithosphere thickness has been varied but crustal thickness and crustal radiogenic heating have been held fixed (at 30 km and 0.50 μW m^{-3}, respectively), showing that increases in lithosphere thickness deepen the isotherms throughout the lithosphere. In order to analyse the possible range in thermal structures in the foreland, we have also performed calculations in which the crustal radiogenic heating has been varied.

We first examine whether our observed earthquake distribution is consistent with the seismogenic thickness tracking the 600 °C isotherm. This temperature has previously been suggested as the upper limit of seismogenic behaviour in anhydrous rocks (of both crustal and mantle lithologies), based upon the comparison of earthquake depths and thermal models (Kohlstedt *et al.* 1995; Mackwell *et al.* 1998; Lund *et al.* 2004; McKenzie *et al.* 2005; Jackson *et al.* 2008, 2021; Priestley *et al.* 2008). We investigate this case first because the New Guinea forelands are comprised at least partially of Proterozoic high-grade metamorphic lithologies of the Australian Shield (Plumb 1979; Hill & Hall 2003), and thus the crust may be anhydrous. We extracted the depth to the 600 °C isotherm from each calculated geotherm. These results are shown in Fig. 6(b), where the depth to the 600 °C isotherm is plotted as a function of lithosphere thickness and radiogenic heating. We then compared these depths to the observed seismogenic thickness of the western and eastern foreland basin, to investigate whether the depth to the 600 °C isotherm represents the maximum possible seismogenic thickness. We chose to analyse the western and eastern halves of the basin separately given the differences in seismogenic and lithosphere thickness. The blue and pink shaded regions show the parameter space over which the depth to the 600 °C isotherm is greater than or equal to the observed seismogenic thickness in the western and eastern foreland basin, respectively, and also where the lithosphere thickness used in our models matches the observed thickness for each side of the basin (Priestley *et al.* 2018).

These results show that the modelled isotherm depth matches the observed seismogenic and lithosphere thicknesses in both halves of the foreland basin. This means that the depth to the 600 °C isotherm can vary laterally by the amount seen in the earthquake depths due to lateral variations in the lithosphere thickness alone, without invoking changes in the composition of the crust. We also note that radiogenic heating in the crust is required to be $\leq$1.5 μW m^{-3}, which is on the lower end of the range of values observed for crustal rocks (Hasterok *et al.* 2018) but consistent with estimates of the overall heat budget of the continental crust (e.g. Rudnick *et al.* 1998; Rudnick & Nyblade 1999; Jaupert *et al.* 2015).

We have also considered the possibility that the foreland basin comprises hydrous crustal material, which would be expected to supported earthquakes only up to temperatures of 350 °C (Chen & Molnar 1983; Priestley *et al.* 2008). Hydrous continental crust might be expected in the eastern foreland basin, on the east side of the Tasman Line, where the geology is comprised of accreted Palaeozoic terranes, instead of the older and thicker Australian craton observed in the west (Crawford *et al.* 2003; Glen 2005). This region east of the Tasman Line may not have been subjected to the partial melting needed to generate anhydrous material. However, our modelling shows that for the depth to the 350 °C isotherm to be consistent with the observed seismogenic thicknesses across the foreland basin, radiogenic heating in the crust would need to be <0.25 μW m^3, which is improbably low (see Fig. S24, which is the equivalent of Fig. 6b, but for the 350 °C isotherm). Thus the seismogenic mid-crust of the eastern foreland is unlikely to be hydrous, despite the presence of overthrust Tasman Orogen units at the surface. These results support our suggestion that the observed lateral variation in seismogenic thickness across the foreland is primarily caused by the change in lithosphere thickness, and not a change in crustal composition. The implications of these results are discussed further in Section 6.1.

4.3 Flexure and elastic thickness

Having investigated the seismogenic thickness and thermal structure of the southern foreland basin, we have also studied its elastic thickness. Elastic thickness is a useful proxy for the strength of the lithosphere as it bends in response to loading, and can be calculated using the wavelength over which this bending occurs, as observed using gravity anomalies. By studying both seismogenic thickness (T_s) and elastic thickness (T_e) of the foreland basin, we aim to contribute to the debate surrounding the rheology of continental lithosphere (e.g., McKenzie & Fairhead 1997; Maggi *et al.* 2000a; Burov & Watts 2006; Jackson *et al.* 2008).

Long-wavelength negative free-air gravity anomalies in the southern foreland basin suggest that the underthrusting Australian Plate is bending as a result of loading from the New Guinea Highlands (Fig. 7a). These gravity anomalies can be used to estimate the effective elastic thickness of the foreland, which we have calculated using the method of McKenzie & Fairhead (1997), which is summarised here. Using the GOCE and EIGEN-6C datasets (Drinkwater *et al.* 2007; Förste *et al.* 2014), the two-dimensional gravity field was stacked into profiles perpendicular to the strike of the range-front. The observed gravity profiles were then compared to synthetic calculations. We invert for the best-fitting value of T_e, while allowing the magnitude and location of the vertical load and bending moment to vary, and also solving for a linear ramp that reproduces any long-wavelength signals in the data that are unrelated to flexure. The elastic thickness estimate obtained using this method is a measure of the effective elastic thickness of the bending layer within the lithosphere, but does not determine the depth to the top or bottom of this layer.

We modelled the west and east sides of the foreland basin separately, as well as calculating elastic thickness across the whole basin. We find the GOCE gravity anomalies between 135.5–141°E can be fit by a plate with an elastic thickness of 5 km, and between 141–143.5°E by an elastic thickness of 6 km (Fig. 7d). Across the whole foreland basin (135.5–143.5°E), T_e is 5 km. Using the EIGEN-6C

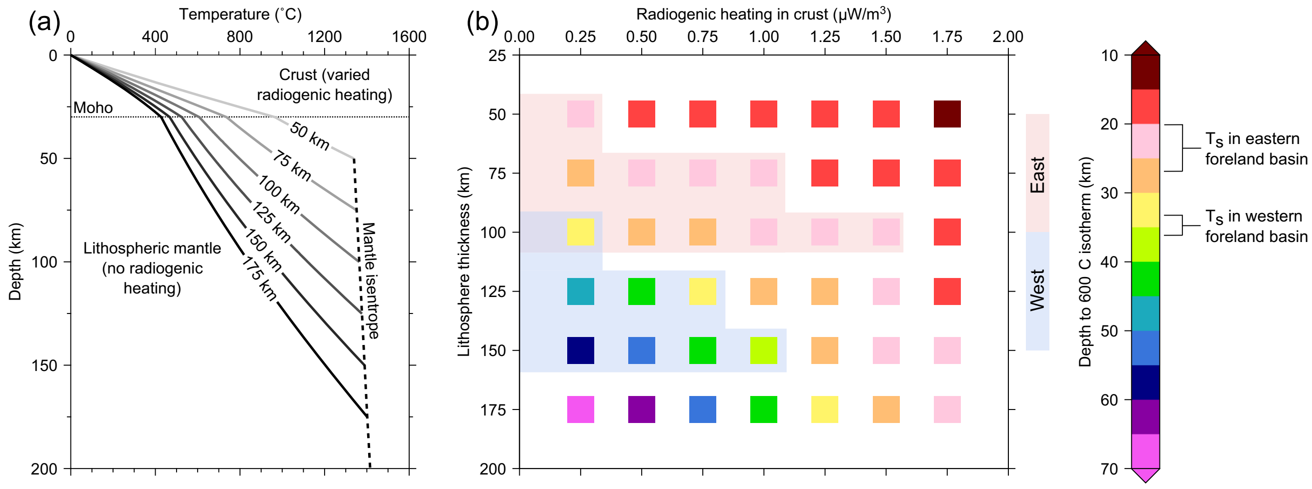

Figure 6. (a) Steady-state geotherms calculated for different values of lithosphere thickness, as indicated. These geotherms were calculated using a crustal thickness of 30 km and constant radiogenic heating in the crust of 0.50 μW m^{-3}, but the radiogenic heating was varied in other models not shown on this plot. (b) Depth to the 600 °C isotherm plotted as a function of lithosphere thickness and radiogenic heating in the crust. The blue region represents the parameter space for the western foreland basin over which the depth to the 600 °C isotherm is greater than or equal to the observed seismogenic thickness (T_s) and the lithosphere thickness is consistent with the results of Priestley *et al.* (2018). The pink region represents the corresponding parameter space for the eastern foreland basin.

dataset, T_e is 5 km between 135.5–141°E, 11 km between 141–143.5°E, and T_e is 6 km across the whole basin. For most of these estimates, the misfit between the modelled and observed gravity anomalies at large T_e values is only slighter greater than the minimum misfit, producing a broad minimum, as can be seen for the eastern foreland basin on Fig. 7(d). This effect is well known, and is caused by trade-offs between T_e, the bending moment, and the location where the vertical load and bending moment are applied (often referred to as the plate break; Jackson *et al.* 2008). When a broad minimum is observed, the upper bound is unconstrained and so our results provide only a lower bound on elastic thickness. Our results do not allow us to robustly use the gravity data to investigate whether there are lateral variations in T_e along-strike of the mountains, so we propose that elastic thickness across the whole foreland basin is ≥5 km.

These results contrast with previous studies of the foreland basin, which found the effective elastic thickness of the underthrusting Australian Plate to be up to 95 km and to vary significantly along-strike (Abers & Lyon-Caen 1990; Haddad & Watts 1999). However these studies held the plate break at a fixed position, which often leads to overestimates of T_e (Jackson *et al.* 2008). The geographical position of the plate break is unknown, thus we prefer to allow the location of the plate break to vary when calculating the misfit. The previous studies also studied single line profiles whereas we chose to stack profiles along-strike of the range, which can lead to more stable results (McKenzie & Fairhead 1997; Jackson *et al.* 2008).

Although some of our estimates are lower bounds on the elastic thickness, some are well-constrained (e.g. the green curve on Fig. 7d). An elastic thickness of <20km is unexpected for a foreland basin setting in which we have observed earthquakes at mid- and lower-crustal depths: in both the western and eastern parts of the New Guinea foreland basin, the effective elastic thickness we have estimated is significantly smaller than the seismogenic thickness inferred from earthquake depths. Estimates of the elastic thickness from other geologically-similar regions have been found to be greater, such as 17–25 km on the eastern foreland of the Andes and in northern India (McKenzie *et al.* 2014, 2015), and Lamb *et al.* (2020) have suggested a global trend in which the elastic thickness is 25–50 per cent of the lithosphere thickness. However, our result is similar to the work of Mitra *et al.* (2018), who studied the Shillong Plateau, a fault-bounded uplift in the foreland basin in the Eastern Himalayas. They determined that the elastic thickness of the Bengal Basin, to the south of the Shillong Plateau, is 5–20 km, which is considerably less than the seismogenic thickness inferred from earthquake depths (40–45 km; Kumar *et al.* 2015). The unusually low elastic thickness estimates from New Guinea and Shillong may therefore relate to either (1) blanketing by large thicknesses of sediment, meaning that large proportions of the cool and shallow crust are occupied by thick piles of (presumably weak) sediments that don't contribute to the elastic strength, or (2) the geological position of both the Shillong Plateau and New Guinea on the continental margin of an underthrusting plate, which may indicate an inherent weakness in these margins. In either case, where constraints can be placed on the upper bound, our estimate of the elastic thickness is less than our observed seismogenic thickness.

4.4 Summary of New Guinea Highlands and forelands

Our results show that there is along-strike variation in seismogenic thickness in the southern foreland basin of the New Guinea Highlands. Thermal modelling suggests that this is likely to be due to lateral variations in lithosphere thickness, rather than crustal composition, such that thicker lithosphere in the west correlates with greater seismogenic thickness. Modelling the gravity anomalies observed in the foreland basin has shown the elastic thickness in both the western and eastern halves of the basin to be small (≥5km, and <20km where the upper bound is constrained), and that $T_e < T_s$ across the whole basin. The implications of these results will be discussed in Section 6.

5 NORMAL FAULTING IN THE BIRD'S HEAD BLOCK

Having studied the present-day tectonics of the New Guinea Highlands and foreland basin, we now turn our attention to the Bird's Head Block of western New Guinea, in order to further investigate the rheology and evolution of the deformation belt. The Bird's Head

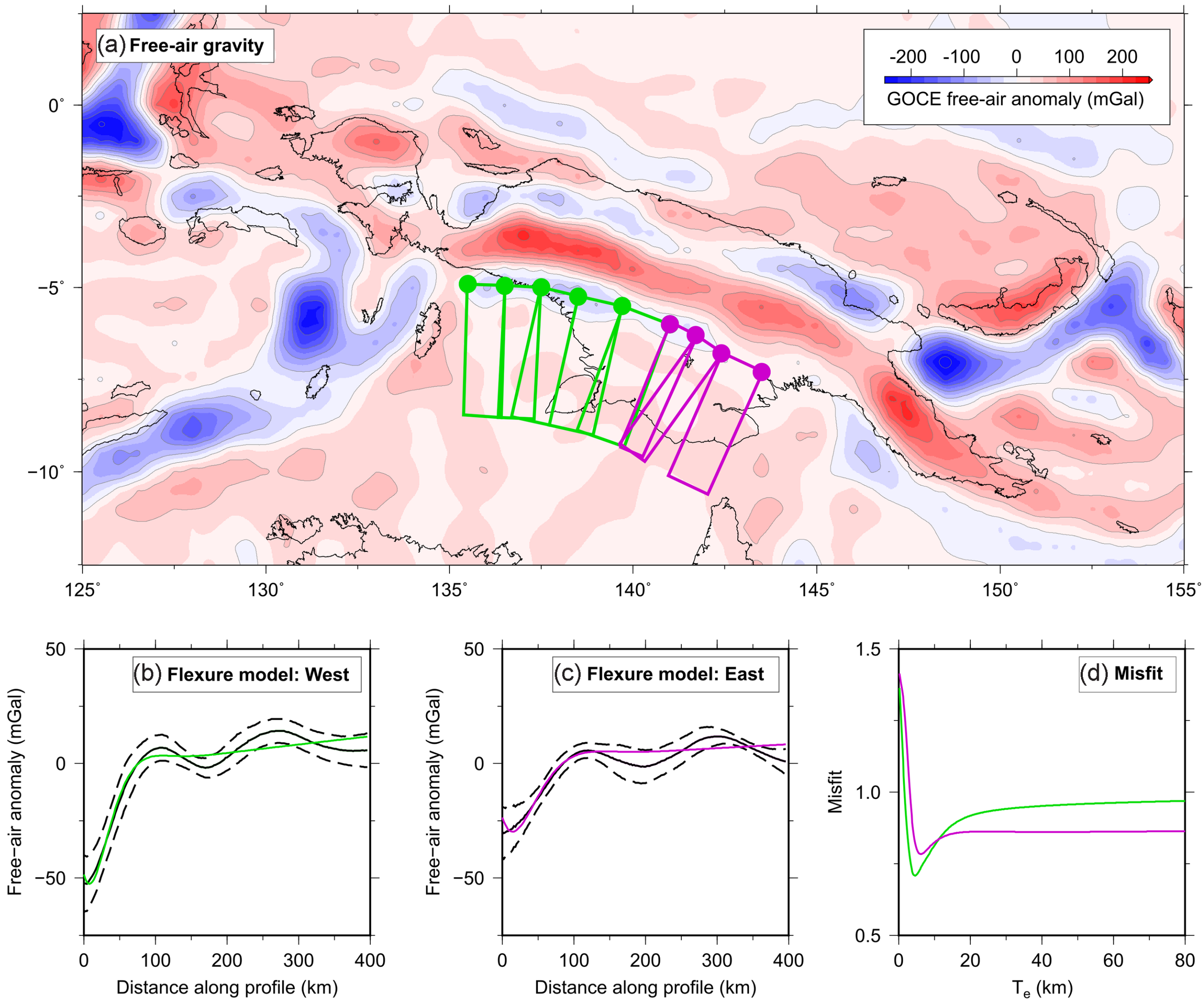

Figure 7. (a) GOCE free-air gravity map of New Guinea (Drinkwater *et al.* 2007). The green and purple coloured boxes represent the region over which profiles through the gravity field, perpendicular to the range front, have been stacked along the length of the west and east foreland basin respectively. The coloured circles represent nodes which have been placed over the gravity minimum. (b and c) Mean (solid black line) and standard deviation bounds (dashed black lines) for the stacked GOCE free-air gravity anomalies, and the best-fitting flexural model to the observed gravity profile (solid coloured line). (d) Weighted misfit between the observed and modelled gravity field, plotted as a function of elastic thickness of the underthrusting Australian Plate. The best-fitting solutions for the west and east occur at $T_e = 4.6$ km and $T_e = 6.2$ km respectively.

Block incorporates the Bird's Head, Neck, and Cenderawasih Bay (Stevens *et al.* 2002; Baldwin *et al.* 2012). We have used earthquake source parameter estimates, seismic reflection profiles, published geodetic results, and geomorphological observations to examine the characteristics of earthquakes in this region, and to study how the regional tectonics may have changed through time.

5.1 Normal faulting

A cluster of normal-faulting earthquakes within the Bird's Neck and the west side of Cenderawasih Bay indicate that the area is experiencing active extension (Figs 3 and 4). Body-waveform modelling and depth-phase analysis we conducted on 5 normal earthquakes in this region have shown that these events are characterised by approximately N-S striking nodal planes and shallow depths of 10 km or less (Table 1 and 2; Fig. 8). These results emphasise the importance of body-waveform modelling and depth-phase analysis to estimate accurate source depths: of the 5 earthquakes we modelled, the ISC-EHB Bulletin lists their depths 25 km deeper on average (Weston *et al.* 2018; International Seismological Centre 2021).

Using the source depths of our modelled earthquakes, we have estimated the seismogenic thickness (T_s) of the Bird's Neck to be approximately 15 km. This estimate of T_s from seismological observations is consistent with the local fault-controlled topography, as the maximum widths of extensional fault-bounded basins have been found to relate to the depth extent of the faults (Jackson & White 1989; Scholz & Contreras 1998). Within the Lengguru Fold-Thrust Belt in the Bird's Neck, high-resolution SRTM 30 m topography data (Farr *et al.* 2007) reveal several fault-bounded basins with a maximum width of 18 km (Fig. 9). The basin width–seismogenic thickness scaling relationship of Copley & Woodcock (2016) yields an estimate of T_s between 12-18 km for that maximum basin width, which is consistent with the seismological estimate. This result also

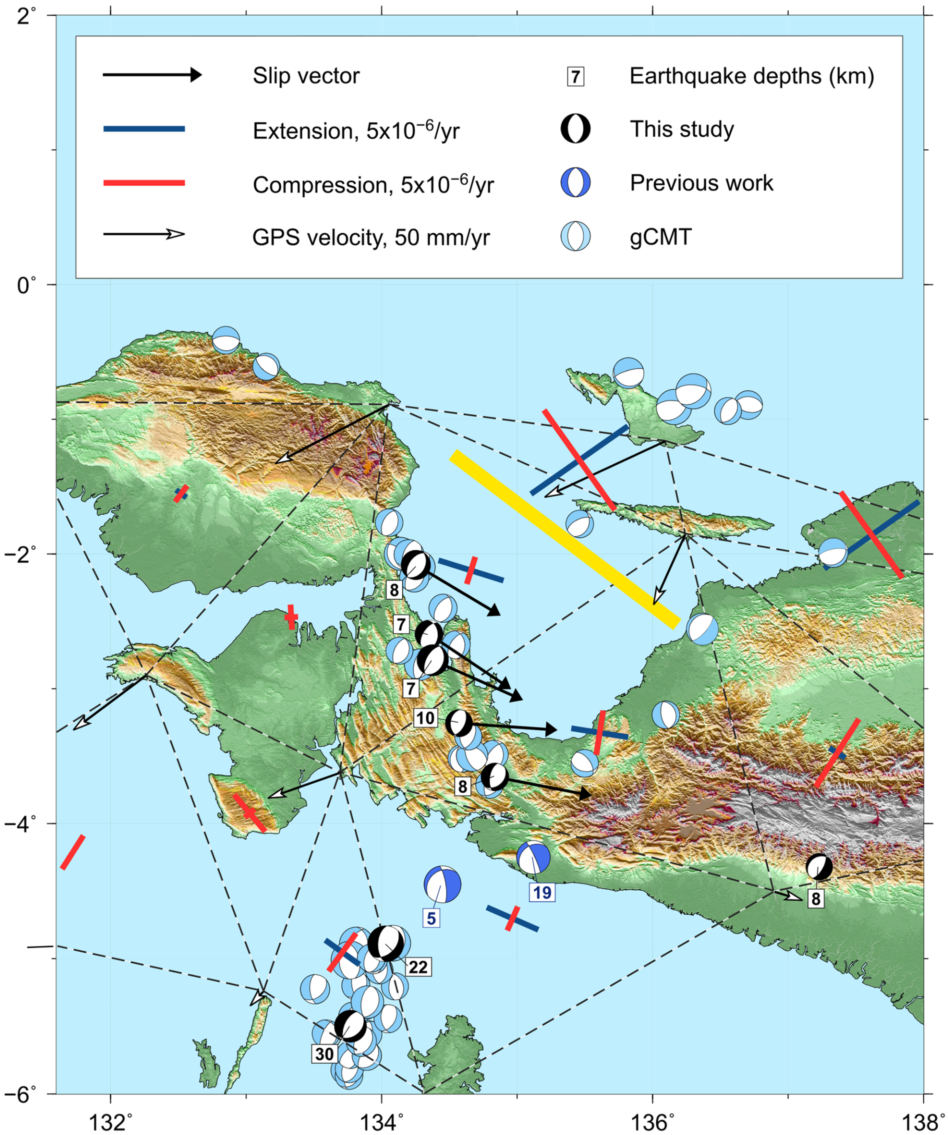

Figure 8. SRTM 30 m DEM overlain with a summary of normal faulting in western New Guinea, showing focal mechanisms, depths, and selected slip vectors of earthquakes determined using body-waveform modelling or depth-phase analysis in this study or previous work (McCaffrey & Abers 1988; Sloan & Jackson 2012). Additional focal mechanisms for normal earthquakes are taken from the gCMT catalogue (Dziewonski *et al.* 1981; Ekström *et al.* 2012). GPS velocities are shown relative to the Australian Plate (Stevens *et al.* 2002). Grey dashed lines delineate the triangulated network of GPS stations from which strain rates were calculated. The yellow line shows the location of the seismic reflection profile shown in Fig. 10.

shows that the Bird's Neck has a lower seismogenic thickness than the foreland basin in central New Guinea. Many studies suggest that the Bird's Head Block represents the northern margin of the Australian continent (e.g., Hamilton 1979; Dow & Sukamto 1984; Hill & Hall 2003). The low seismogenic thickness might result from the Bird's Neck representing a thinned continental margin, or because the Palaeozoic metasediments which comprise the basement geology are likely to be weaker than the Precambrian craton which underlies the western foreland basin in central New Guinea (Visser & Hermes 1962; Pieters *et al.* 1983; Bailly *et al.* 2009).

To further study the nature of extension in western New Guinea, we have estimated geodetic strain rates across the region using the triangulation method of Bourne *et al.* (1998) and the GPS data of Stevens *et al.* (2002). This method was selected because the GPS network across New Guinea is sparse, and so it is more suitable to calculate strain rates within discrete triangles than to calculate strain rate as a continuous field. The region of interest was split into triangles with a GPS site located at each vertex. The strain rate within each triangle was calculated via a linear, piecewise continuous interpolation across the triangular region, using the three GPS velocities. The strain rate within each triangle is equal to the average strain rate obtained from a continuous strain rate field over the same region, and is independent of the choice of geodetic reference frame. Our geodetic analysis is shown in Fig. 8, alongside a summary of normal faulting in western New Guinea. The GPS data show that the Bird's Head Block is moving rapidly with respect to the Australian Plate. The strain rate analysis matches our observations of seismicity across the region: extension occurs approximately E-W across Cenderawasih Bay, the Bird's Neck, and further south towards the Aru Trough. Rapid left-lateral shear strain is also observed across the north coast of the island, coincident with the location of the Sorong and Yapen Fault Zones. We find that

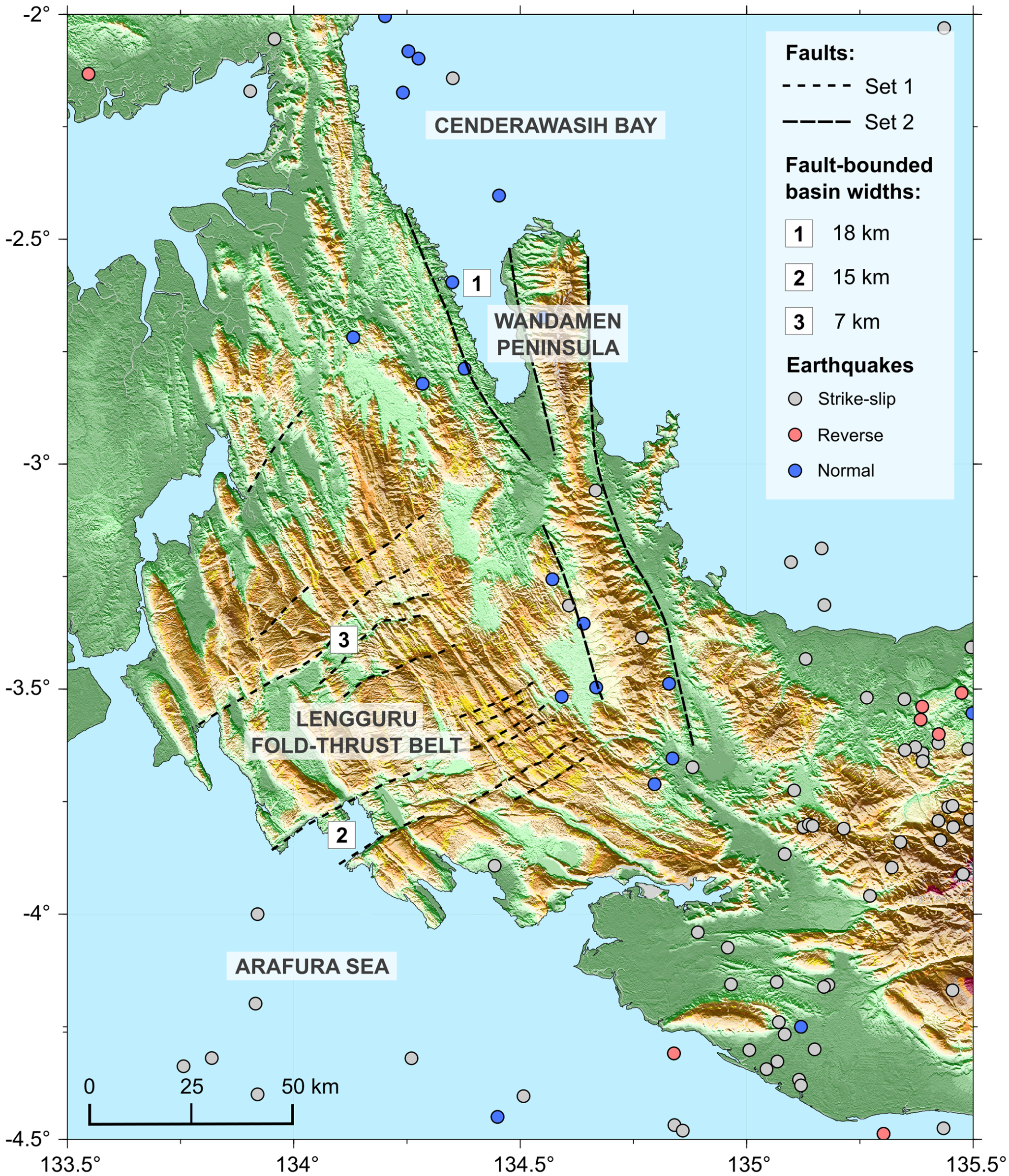

Figure 9. SRTM 30 m DEM of the Bird's Neck region. Normal faults are shown as dashed black lines. The width of fault-bounded basins are also indicated. Earthquake hypocentres from the gCMT catalogue are coloured according to focal mechanism.

the orientation of extensional strain on the west side of Cenderawasih Bay is consistent with the calculated slip vectors for normal earthquakes in the region, such that the extension is most likely accommodated by slip on these shallow normal faults. We note that the smaller component of ∼N-S compression in the region may be related to locking on the megathrust to the north (but that this source of deformation would be unable to reproduce the observed ∼E-W extension). Because the errors on the GPS velocity estimates (2–3 mm/yr) are small compared with the velocity differences across the triangles (up to 125 mm/yr), these results are robust.

5.2 Tectonic changes through time

Whilst the Bird's Neck and Cenderawasih Bay are currently experiencing E-W extension, topographic structures imply that the region has undergone several stages of tectonic deformation during the Neogene. The Lengguru Fold-Thrust Belt (LFTB) within the Bird's Neck comprises anticlinal folds striking approximately NW-SE, formed of Mesozoic shelf sediments from the Australian passive margin above Palaeozoic metasedimentary basement (Fig. 9; Visser & Hermes 1962; Dow & Sukamto 1984; Bailly *et al.* 2009). Analysis of offshore seismic lines and petrological analysis of metamorphic rocks from Wandamen Bay has constrained the timing of formation of the LFTB to between 11–2 Ma (Bailly *et al.* 2009; François *et al.* 2016; White *et al.* 2019).

Using the SRTM 30 m DEM, we have identified two groups of normal faults in the Bird's Neck (Fig. 9). One set of faults in the southwest of the Bird's Neck strike NE-SW and cut across the LFTB at a high angle (Set 1). Anticlines which are cut by these faults show vertical offsets in the topography of 150–700 m. There appear to be no recent earthquakes associated with these faults within the fold-thrust belt. However, the clear geomorphological expression of these faults suggests that it is possible the faults are active, and the lack of seismicity could be due to the combination of low strain rates and the length of the instrumental earthquake catalogue. A second set of normal faults near the Wandamen Peninsula strike approximately N-S and may be associated with the recent normal-faulting earthquakes along the west side of Cenderawasih Bay (Set 2). These normal faults run parallel to the major anticline which forms the Wandamen Peninsula, so these faults may represent reactivated thrust faults from the formation of the LFTB, or from the emplacement of the Weyland Overthrust: a block of metamorphosed sediments and ophiolite slices which was thrust ∼25 km southwest in the late Miocene (Dow & Sukamto 1984; Bailly *et al.* 2009; François *et al.* 2016). The change in fault orientation between Set 1 and Set 2 may represent a change in the direction of strain being experienced within the Bird's Neck in either space or time. It has also been suggested that movement of the Bird's Head Block relative to Australia may be at least partially accommodated by vertical axis rotations of large crustal blocks (Stevens *et al.* 2002). This theory might explain the discrepancy between the orientation of the geomorphologically-clearest faults in Set 1 (striking NE-SW) and the focal mechanisms of the recent normal earthquakes (striking N-S and with slip vectors aligned with the extensional principal axes calculated from the GPS data).

To further investigate the timing of tectonic changes in the region through time, we have analysed a seismic reflection profile in the north of Cenderawasih Bay (line location indicated in Fig. 8). This seismic line was originally presented by Priastomo (2012), and we have updated the ages of the main horizons using the results of Babault *et al.* (2018). In the northwestern part of the seismic reflection profile, the data show a fold-and-thrust system which has deformed the Oligocene-Miocene sedimentary sequence (Fig. 10). This period of shortening appears to have ended by 3.6 Ma, as shown by the undeformed covering of sediments of this age (blue dotted horizon in Fig. 10 above the folds; Priastomo 2012). The sedimentary sequence has then been displaced by extensional faults that appear to be active at present. Fault A (indicated in Fig. 10) has a prominent bathymetric expression, with ∼1.5 km relief (equivalent to ∼2 seconds two-way travel time) and with apparently larger displacements in the underlying sedimentary units. Fault B shows growth in the uppermost parts of the stratigraphy, including a horizon dated at ∼63–480 ka (orange dotted line; Babault *et al.* 2018). Sedimentary growth is seen only in the uppermost units of the Pliocene-Recent sequence. These observations indicate a tectonic change from compression to extension occurred in this region at some time after 3.6 Ma.

In the southeastern part of the seismic reflection profile, the seismic horizons are affected by NE-SW trending folds and thrust faults, which are rooted in a detachment within the Pliocene-Quaternary sedimentary column (Decker *et al.* 2009; Priastomo 2012; Babault *et al.* 2018). This region has been named the Cenderawasih Fold-and-Thrust Belt (Priastomo 2012) or Waipoga Fold-and-Thrust Belt (WFTB; Babault *et al.* 2018). Rather than representing tectonic deformation, the WFTB is interpreted as a toe-thrust system resulting from gravitational instability in the external part of the sedimentary prism, which is up to 12 km thick and where sedimentation rates could have reached very high values during the last 3 My (Babault *et al.* 2018). The WFTB formed after the LFTB in the Bird's Neck, and the base of the syn-tectonic sediments is dated at ∼63–480 ka (Babault *et al.* 2018). Hence, deformation in the WFTB is probably no older than late Pleistocene. The seismic reflection profile shows that compressive folding and thrusting in the upper sedimentary sequence in this area does not affect the lower sedimentary sequence and basement. This is consistent with the interpretation of the shortening being due to localized gravitational instability within the sedimentary pile, rather than representing crustal-scale tectonic deformation. We discuss below the implications of the changing tectonic configuration through time in the region of the Bird's Neck and Cenderawasih Bay.

6 INTERPRETATIONS AND DISCUSSION

6.1 Reconciling observations of earthquake depths, lithosphere thickness and elevation

Body-waveform modelling and depth-phase analysis of earthquakes in the New Guinea foreland basin has shown that the seismogenic thickness of the foreland varies along-strike, being greater in the west than the east. This variation in seismogenic thickness correlates with an along-strike variation in lithosphere thickness, derived from surface wave tomography, such that thicker lithosphere is observed in the areas of greater seismogenic thickness (Fig. 5; Priestley *et al.* 2018). Using simple thermal modelling techniques, we have shown that the variation in seismogenic thickness in the foreland basin can be attributed solely to the changing lithosphere thickness, without having to invoke any variation in other parameters such as crustal composition. The 600 °C isotherm, which is commonly thought to represent the depth extent of earthquakes in anhydrous continental crust (e.g. Jackson *et al.* 2021), is located deeper in thicker lithosphere and thus allows earthquakes to occur at greater depths.

It is surprising that the seismogenic thickness in the eastern part of the foreland appears to be governed by the 600 °C isotherm, given that, in contrast to the high-grade and anhydrous metamorphic rocks and thick lithosphere that usually characterize where earthquakes occur at such high temperatures (Mackwell *et al.* 1998; McKenzie *et al.* 2005; Jackson *et al.* 2021), the region has relatively thin lithosphere and is believed to be formed of accreted island arc, back arc, and forearc terranes of the Tasman Orogen (Crawford *et al.* 2003; Hill & Hall 2003; Glen 2005). Within these accreted terranes, it might be expected that earthquakes in the eastern foreland would be limited to material at temperatures <350 °C, as is observed in regions of hydrous crust which have not undergone partial melting (Priestley *et al.* 2008). However, as described in Section 4.2, for reasonable values of radiogenic heating, the observed seismogenic thickness in the eastern part of the foreland is much greater than the depth to the 350 °C isotherm calculated from our thermal modelling. We suggest that the observed seismogenic thickness may be due to two factors. First, the Tasman Orogen was formed in the Palaeozoic above a west-dipping subduction zone, and oceanic terranes were progressively thrust over and onto the Precambrian rocks of the Australian continental interior (Coney *et al.* 1990; Veevers 2000; Crawford *et al.* 2003; Glen 2005). It is therefore possible that the strong, anhydrous, high-grade metamorphic rocks of the Australian craton form the mid-to-lower crust in the eastern New Guinea foreland, which have been overthrust by the Tasman Orogen. This suggestion is supported by Aitchison *et al.* (1992), who analysed zircons from the basement of the New England Orogeny in eastern Australia and concluded that terranes of the Tasman Orogen have been 'thrust a considerable distance over the continental freeboard of eastern Australia'. Secondly, east–west rifting along the northeastern margin of the Australian continent in the late Cretaceous-early Eocene, which formed the Coral Sea (Fig. 1b), is likely to have thinned the lithosphere along this margin (Weissel & Watts 1979; Davies *et al.* 1997; Gaina *et al.* 1999).

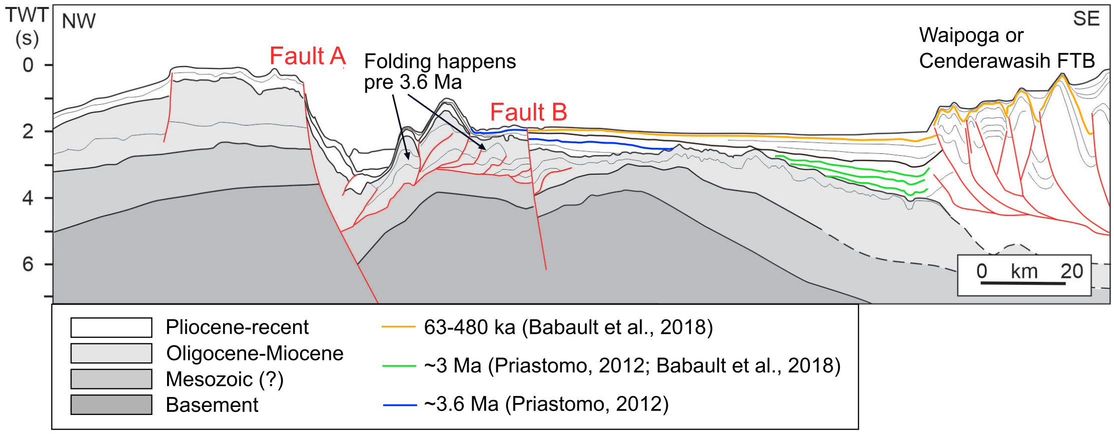

Figure 10. Interpretation of 2D seismic reflection profile CE07-17 across Cenderawasih Bay, modified after Priastomo (2012). The location of the seismic line is shown in Fig. 8. The age of the horizons is from Priastomo (2012) and Babault *et al.* (2018). Decker *et al.* (2009) and Sapiie *et al.* (2010) interpreted the lower sequence as syn- and post-rift passive margin sediments (mid and light grey units in the figure) overlying a basement (darker grey). Slip on fault B happens post 3.6 My. In the Waipoga Fold-and-Thrust Belt, the base of the syn-tectonic sediments is dated at ∼63–480 ka (Babault *et al.* 2018).

These two factors combined could result in anhydrous and seismogenic mid-to-lower crust in a region of thin lithosphere, with an absence of high-grade anhydrous rocks at the surface. This situation would allow for earthquake depths across the whole foreland basin to be limited by the depth to the 600 °C isotherm, the location of which is controlled by lithosphere thickness and the resulting temperature structure.

An additional observation to consider is the elevation of the New Guinea Highlands. There is a long-established concept that the maximum height that can be achieved by a mountain range depends on the strength of the bounding forelands (Dalmayrac & Molnar 1981; England & Houseman 1988; Molnar & Lyon-Caen 1988). Therefore we might expect the western Highlands to have a significantly higher elevation than the east, due to the thicker, cooler and stronger foreland. However, in New Guinea, although the seismogenic and lithosphere thickness vary and correlate along-strike, the elevation of high, low-relief plateau-like regions of the mountain range are very similar in the east and west (Fig. 5b). This consistency might be explained if the mountains have not yet reached their limiting elevation (the maximum elevation which can be supported by the forelands). However, the Highlands show little evidence of active crustal thickening (Fig. 4); instead the thrust faulting has stepped southwards into the range front (Fig. 3; Visser & Hermes 1962; Hamilton 1979; McCaffrey & Abers 1988). This observation suggests that the New Guinea Highlands have reached their current limiting elevation. The low-relief interior of the ranges implies that their elevation is not controlled by erosion, in which case they would be characterised by actively incising drainage. The lack of correlation between elevation and seismogenic thickness therefore warrants an explanation.

To examine how the mountain range elevation might be related to the thickness and thermal structure of the underthrusting lithosphere, we have calculated the forces acting between the New Guinea Highlands and forelands. Mountains have a higher gravitational potential energy than their forelands, due to the work done against gravity when thickening the crust. The horizontal force per unit length exerted between a mountain range and its foreland, caused by this contrast in potential energy, can be calculated from the lateral differences in density structure between the two regions (Artyushkov 1973; Dalmayrac & Molnar 1981).

We consider the New Guinea Highlands and forelands as isostatically balanced columns which have a vertical density structure controlled by the temperature, composition and thickness of the crust and lithospheric mantle. Lateral differences between these density structures will generate horizontal gradients in vertical normal stress. By integrating the vertical normal stress from the surface to the depth of isostatic compensation, we can obtain the horizontal force per unit length acting between the mountains and the forelands (Artyushkov 1973; Dalmayrac & Molnar 1981). We assume that the New Guinea Highlands have reached the maximum elevation which can be supported by the forelands, because the mountains are dominated by strike-slip faulting and the reverse faulting has migrated into the foreland basin (Fig. 3). This assumption allows us to use the potential energy contrasts to explicitly estimate the horizontal force exerted on the forelands (Dalmayrac & Molnar 1981).

We performed separate calculations for the western and eastern regions, separated at 141°E, due to the observed along-strike variation in lithosphere thickness. Following the methods of Copley & Woodcock (2016) and Wimpenny *et al.* (2018), which are built upon Lamb (2006), we have varied the model parameters throughout the range of geologically plausible values in order to estimate a range of possible force magnitudes (Table 3), as described here. To calculate the vertical density structures, we take the crustal thickness in the forelands to be 30–35 km, based on receiver function studies in the Arafura Sea (Jacobson *et al.* 1979; Clitheroe *et al.* 2000), and 40–60 km in the mountains, where the value is less constrained (Abers & McCaffrey 1988; Abers & Roecker 1991). Lithosphere thickness is taken from the measurements of Priestley *et al.* (2018). Geotherms in both the mountains and forelands were assumed to be in steady state, and consist of 2 linear sections between the surface and the Moho, and the Moho and the base of the lithosphere (which is enforced to be at the isentropic temperature, given a mantle potential temperature of 1315 °C). Estimates of Moho temperature in the forelands were derived using the geotherms calculated in Section 4.2 and the estimates of crustal thickness. Moho temperatures in the mountains were varied over a wide range to account for uncertainties in thermal structure and crustal thickness estimates. The average density (at 0 °C) of the crust in the forelands and mountains was taken to be 2800 kg m $^{-3}$ (Turcotte & Schubert 2002). We used a thermal expansion coefficient of 3×10^{-5} K^{-1} to model

Table 3. Parameters used to calculate the horizontal force exerted between the New Guinea Highlands and forelands, and to estimate the frictional strength of crustal faults in the foreland basin. The parameters taken from Karato & Wu (1993) are for a dry olivine dislocation creep law: $\Delta\sigma_{xx} = S\dot{\epsilon}_r^{\frac{1}{n}} A^{\frac{-1}{n}} exp(\frac{E+PV}{nRT})$, where $\Delta\sigma_{xx}$ is the differential stress, S is the shear modulus, $\dot{\epsilon}$ is the reference strain rate, A is a constant, n is the power law exponent, E is the activation energy, P is pressure, V is the activation volume, R is the gas constant and T is temperature.

Variable	Value		Source
	West	East	
Crustal thickness (lowlands)	30–35 km	30–35 km	Jacobson *et al.* (1979); Clitheroe *et al.* (2000)
Crustal thickness (mountains)	40–60 km	40–60 km	Abers & McCaffrey (1988); Abers & Roecker (1991)
Lithosphere thickness (lowlands)	100–150 km	50–100 km	Priestley *et al.* (2018)
Lithosphere thickness (mountains)	100–160 km	50–110 km	Priestley *et al.* (2018)
Moho temperature (lowlands)	400–600 °C	550–800 °C	This study
Moho temperature (mountains)	500–800 °C	600–1000 °C	This study
Foreland seismogenic thickness	33–36 km	20–27 km	This study
Foreland sediment thickness	1.5–5 km	0.1–1.5 km	Visser & Hermes (1962)
Foreland fault dips	27–87°	15–75°	This study
Relief	2–3 km	1.5–2.75 km	This study
Mantle potential temperature	1315 °C		McKenzie *et al.* (2005)
Thermal expansivity of crust	3×10^{-5} K^{-1}		Turcotte & Schubert (2002)
Thermal expansivity of mantle	$3–4.5 \times 10^{-5}$ K^{-1}		Bouhifd *et al.* (1996)
Asthenosphere density (p_a, 0 °C)	3300 kg m^{-3}		Turcotte & Schubert (2002)
Lithosphere mantle density (0 °C)	p_a - 60 kg m^{-3}		Turcotte & Schubert (2002)
Crustal density	2800 kg m^{-3}		Turcotte & Schubert (2002)
Pre-exponential factor (A)	3.5×10^{22} s^{-1}		Karato & Wu (1993)
Activation energy (E)	540 kJ mol^{-1}		Karato & Wu (1993)
Activation volume (V)	20 cm^3 mol^{-1}		Karato & Wu (1993)
Stress exponent (n)	3.5		Karato & Wu (1993)

the density changes in the crust caused by temperature (Turcotte & Schubert 2002). The density of the lithospheric mantle is taken to be 60 kg m^{-3} less than the density of the asthenosphere at the same P–T conditions. We used the results of Bouhifd *et al.* (1996) to model the thermal expansion of the lithospheric mantle.

By varying all input parameters, we estimate that the horizontal force exerted between the western Highlands and foreland is 2.5–5 $\times$ 10^{12} N m^{-1} along-strike of the range, and 2–4.5 $\times$ 10^{12} N m^{-1} between the eastern Highlands and forelands (Fig. 11a), therefore showing little along-strike variation. This situation is to be expected, because generally the horizontal force exerted between a mountain range and its lowlands scales with elevation. For example, the forces across the New Guinea Highlands are larger than those calculated for the mountains of Albania (1.2 $\times$ 10^{12} N m^{-1}; Copley *et al.* 2009), where mean elevation is only ∼1 km compared to 2–3 km in New Guinea. However in the Andes, where elevation is 4–5 km, the horizontal force between the Andes and South American lowlands is 4–8 $\times$ 10^{12} N m^{-1} (Wimpenny *et al.* 2018), which is larger than the forces seen in New Guinea.

To reconcile our observations of seismogenic thickness, thermal structure and elevation, we propose that the current elevation of the Highlands has been set by the thin passive margin material on the northern margin of the Australian Plate which was involved in the initial stages of the orogeny. Mountain building began around 15 Ma, with the northwards underthrusting of thin continental lithosphere from the northern passive margin of Australia. Triassic rifting along this northern margin had truncated the Tasman Orogen in eastern New Guinea, and formed a ∼1000 km wide shelf underlain by thinned continental crust (Pigram & Panggabean 1984; Cloos *et al.* 2005). Thus the initial stages of mountain building presumably involved the underthrusting of lithosphere that would have been thinner, hotter, and weaker than that now underthrusting the western part of the range (Fig. 12). Only recently has thicker continental crust and lithosphere from the Australian Plate been underthrusting the mountains (beginning 10–8 Ma; Cloos *et al.* 2005), with cold, strong cratonic material in the west but the continued underthrusting of thinner, weaker lithosphere in the east due to the along-strike variability in the lithosphere structure. It is likely that crustal thickness and elevation in the Highlands have not yet readjusted to the arrival of stronger material in the west and have not reached the maximum elevation as can be supported by the stronger forelands. Over time, we expect the elevation of the western Highlands to grow in response to the increased strength of the cold cratonic foreland crust (Fig. 12). This concept highlights the possible effects of lateral variations in lithosphere strength on the evolution of topography during the initial stages of mountain building.

The New Guinea Highlands have lower elevation than long-lived mountain ranges like the Andes (∼4 km) and the Tibetan Plateau (4–5 km). Despite the underthrusting material increasing in strength over time, the current New Guinea foreland also has a lower seismogenic thickness and elastic thickness than northern India and the Andean foreland (e.g. Assumpção & Suárez 1988; McKenzie & Fairhead 1997; Maggi *et al.* 2000a; Pérez-Gussinyé *et al.* 2007; McKenzie *et al.* 2014). These comparisons emphasize the importance of spatial variability in the underthrusting plate in controlling the evolution of the bounding mountain ranges, for while northern India and the Andean foreland represent strong continental interiors, New Guinea represents a weak continental margin which supports lower elevation mountains. However, as more Australian material is underthrust and the forelands gradually come to be composed of strong continental interior (e.g. the region in the central Arafura Sea which supports upper mantle earthquakes at 61 km depth; Sloan & Jackson 2012), the New Guinea Highlands may eventually reach elevations similar to the Andes and Tibet.

6.2 Foreland deformation and fault strength

There are two lines of evidence which suggest that the western and eastern New Guinea foreland are deforming differently. First,

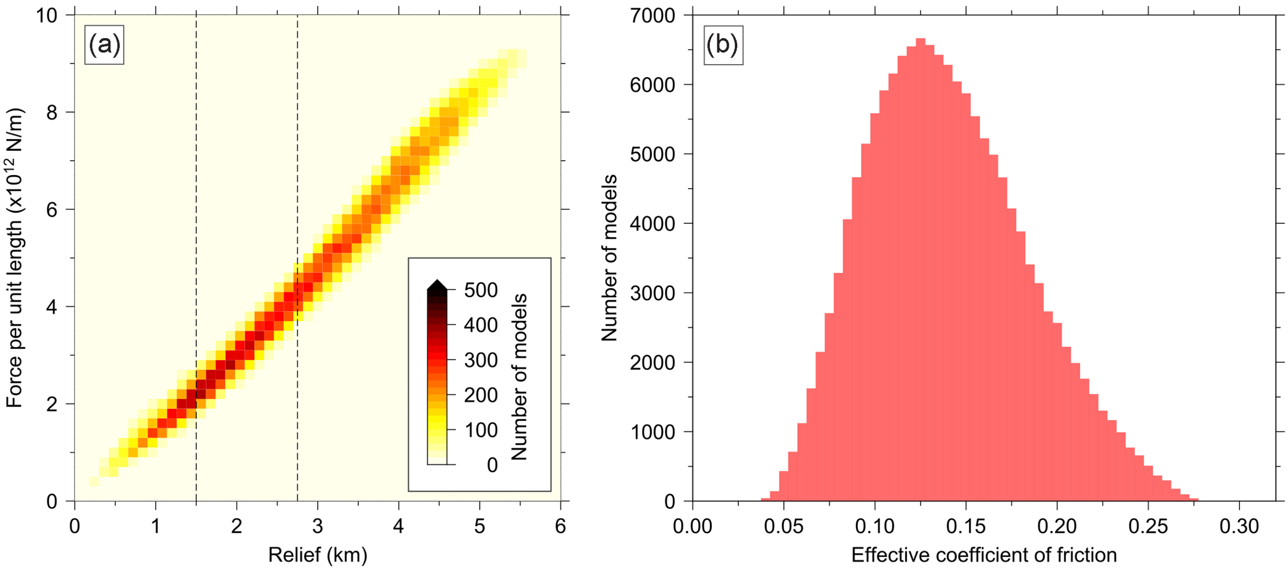

Figure 11. (a) Results of calculations for force per unit length transmitted through the lithosphere due to gravitational potential energy differences between the eastern New Guinea Highlands and forelands. The transmitted force was calculated by varying lithosphere thickness, crustal thickness, and temperature structure. Force per unit length is shown as a function of relief between the mountains and lowlands. The vertical black dashed lines represent the range of appropriate solutions given the range of relief observed in the eastern New Guinea Highlands. (b) Estimates of the effective coefficient of friction on crustal faults in the east foreland basin. Calculations have assumed the entire crust is in compression and that the lithosphere mantle deforms via dislocation creep at temperatures above 600 °C.

there are broad-scale differences in the topography of the foreland basin. In the east lies the Darai Uplift, which is situated south of the range front (Fig. 1b). Also referred to as the Darai Plateau or Darai Anticline, this structure is 150 km long and reaches a maximum elevation of ∼1 km above the surrounding foreland. The Darai Uplift is a single basement-cored anticline which is thought to represent shortening on a major basement-involved thrust fault, which itself may be a reactivated extensional fault generated by Mesozoic passive margin rifting (Hobson 1986; Hill 1991; Buchanan & Warburton 1996). In contrast, the western foreland basin shows no large-scale structures comparable to the Darai Uplift and appears to be mostly 'unbroken'. The overlying fold-thrust belt appears to be relatively thin-skinned, and consists primarily of en echelon folding with kilometre-scale subsidiary thrust faulting (Granath *et al.* 1991; Cloos *et al.* 2005).

The second line of evidence concerns active faulting in the foreland basin. Our earthquake modelling has revealed high-angle reverse faulting earthquakes with nodal planes striking parallel to the range front (Fig. 3). In the western foreland basin between 135 and 141.5°, it does not appear that the earthquakes are breaking through the entire seismogenic foreland. The isolated M_w 5.2 earthquake at 33 km depth in the western foreland is separated from the shallower events by an apparently aseismic middle crust, and the deep event is not large enough to have ruptured the entire seismogenic layer. In contrast, the eastern foreland basin between 141.5° and 145° contains earthquakes for which the depths span the whole of the seismogenic layer. In conjunction with the presence of the Darai Uplift in the eastern foreland basin, these observations imply that the force being exerted between the mountain range and the Australian foreland is large enough to break the entire thickness of the crust in the eastern foreland basin, but not in the west. This pattern is consistent with our logic described above that the western foreland is stronger than the east because of the thicker lithosphere leading to cooler temperatures in the crust and a thicker seismogenic layer.

For reverse faulting to occur throughout the crust in the eastern foreland, the horizontal compressive forces acting between the Highlands and forelands must be large enough to exceed the static frictional strength of the faults. In this setting, we are therefore able to estimate the rheology of these faults (Copley *et al.* 2011). In contrast, where the foreland is not deforming, although the type of analysis shown in Fig. 11(a) can estimate the force transmitted through the foreland, it is only possible to place a lower bound on the fault strength. In order to estimate the frictional properties of the faults breaking the eastern New Guinea foreland, we have followed the method of Wimpenny *et al.* (2018) by constructing 1-D yield stress profiles which represent the stress state with depth. By integrating the yield stress over depth, we can estimate the force per unit length which the foreland lithosphere can support ($F = \int \Delta\sigma_{xx}\, dz$; where F is force per unit length, $\Delta\sigma_{xx}$ is horizontal differential stress, and z is depth). We have undertaken this process for a range of different rheological parameters, as described below. By comparing the forces estimated by these calculations with our estimate of the horizontal force exerted between the mountains and lowlands as described above, we can place an upper bound on the frictional strength of faults in the eastern New Guinea forelands.

We performed a parameter sweep through the range of variables which control the shape of the yield stress envelope with depth, as listed in Table 3 (sediment thickness, seismogenic thickness, fault dip, neutral fibre depth, elastic core thickness, and effective coefficient of friction). As with the force calculations above, this process was undertaken due to the uncertainty in the values of some variables. We have also considered the creep strength of the lithospheric mantle in our calculations, as follows. Earthquake source modelling has shown that there is little evidence for deep earthquakes occurring within the foreland mantle lithosphere (Fig. 5). This observation, and the comparison between the seismogenic and elastic thickness estimates described above, suggest that the horizontal forces are mostly supported by frictional stresses within the

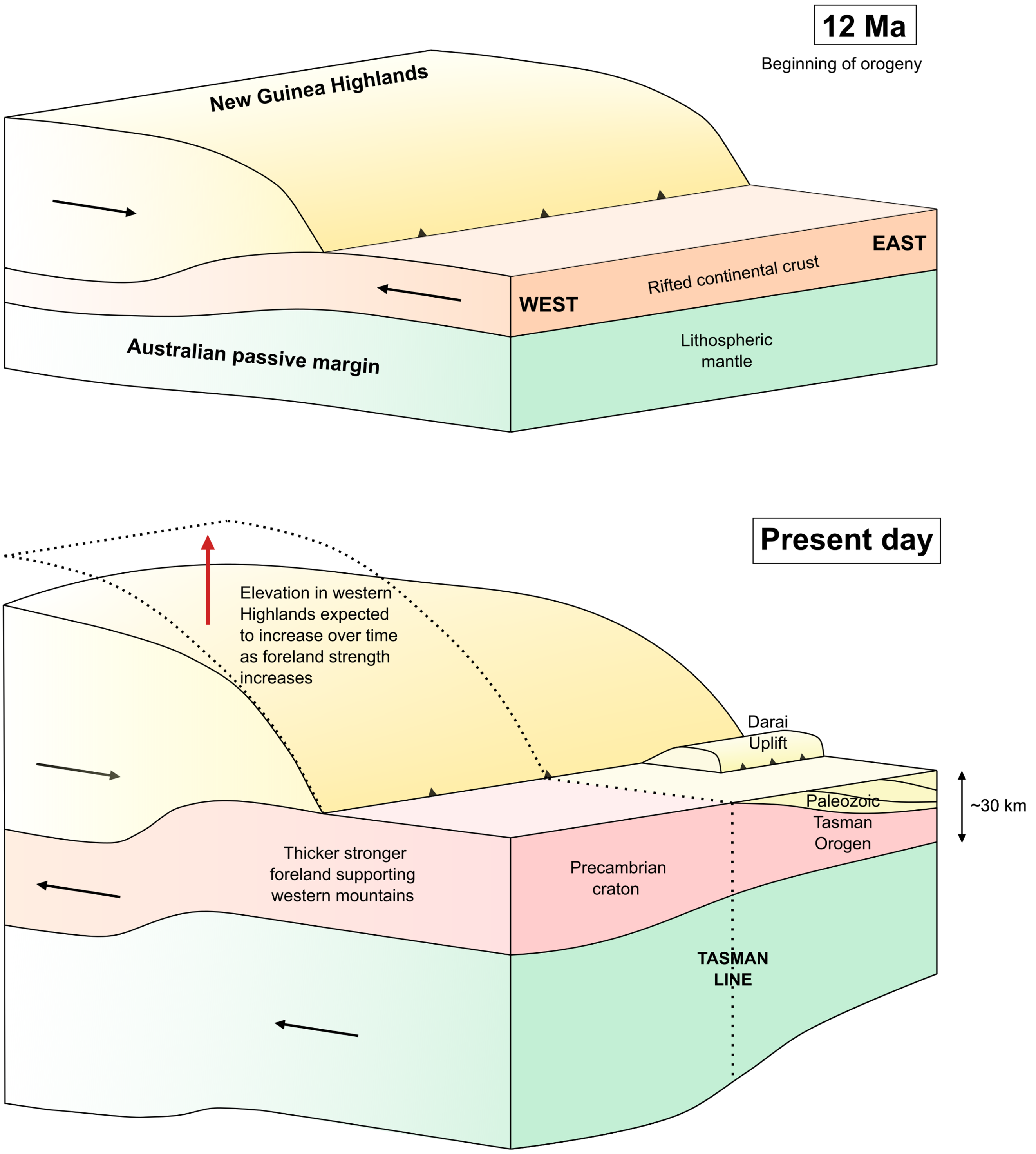

Figure 12. Schematic diagram of the New Guinea Highlands showing how the lithosphere and mountain elevation has evolved since the beginning of the orogeny, and how it may be expected to evolve over time due to changes in the rheology of the underthrusting Australian Plate.

seismogenic crust. We assume that at temperatures above 600 °C, the mantle deforms mostly by ductile creep. We use a dry olivine dislocation creep law (Karato & Wu 1993), which gives an upper bound on the ductile strength of the lithospheric mantle and thus a lower bound on the frictional strength of crustal faults. At temperatures <750 °C, it has been suggested that the upper mantle may deform plastically via Peierl's Creep (Mei *et al.* 2010; England & Molnar 2015), which gives a lower estimate of ductile mantle strength than when dislocation creep is assumed. However, we have also performed calculations in which the lithospheric mantle has zero strength, which gives an absolute upper bound on the frictional strength of crustal faults.

Our results show that in order to break in response to the 2–4.5 $\times$ 10^{12} N m^{-1} horizontal force transmitted between the mountains and the foreland, the effective coefficient of friction for crustal faults in the eastern New Guinea forelands must be <0.28, if we assume the lithospheric mantle deforms by dislocation creep above 600 °C (Fig. 11b). These coefficients of friction are equivalent to depth-averaged differential stresses of ≤104 MPa. The nominal most likely value for the effective coefficient of friction is 0.125, equivalent to a depth-averaged differential stress of 46 MPa. If the lithospheric mantle supports no stress whatsoever, the maximum effective coefficient of friction in the forelands is 0.31 (corresponding to depth-averaged differential stresses of ≤115 MPa).

In the western foreland basin, we do not see evidence for basement-cored anticlines and the earthquakes are not distributed throughout the crust (Fig. 5). Thus the crust does not appear to be breaking through on faults in the same way as in the eastern foreland basin. The western foreland must therefore be strong enough to support the horizontal forces exerted between the mountains and the lowlands, which we estimated to be $2.5–5 \times 10^{12}$ N m^{-1} along-strike. Therefore, the strength of these faults in the western foreland cannot be estimated, and only a lower bound placed upon this value (i.e. that we know they must be strong enough to not deform in response to the applied forces). Using the same frictional analysis as for the eastern foreland, we can therefore calculate the minimum coefficient of friction needed to support the observed horizontal forces. Our analysis shows that the lower bound on the effective coefficient of friction in the western foreland is between 0.01 and 0.14. It is likely that faults in the western and eastern foreland have similar strength, but the greater seismogenic thickness of the western foreland allows it to support the horizontal force (which is very similar across the east and west forelands) without breaking. Assuming fault strength is similar across the foreland basin and that the mantle deforms via dislocation creep, we can therefore constrain the effective coefficient of friction of faults in the New Guinea foreland to be between 0.01 and 0.28.

Our results are consistent with similar studies of foreland regions, which found low estimates of the effective coefficient of friction in the Variscan forelands (<0.24; Copley & Woodcock 2016), the Peruvian Andes (<0.15; Wimpenny *et al.* 2018), and the northern Indian shield (<0.3; Bollinger *et al.* 2004; Herman *et al.* 2010; Copley *et al.* 2011). While these geophysical studies show consistent results, they are significantly lower than traditional laboratory estimates of dry rock friction (0.6–0.8; Byerlee 1978). This suggests that the foreland faults may be weak because they are reactivated structures containing phyllosilicate-rich fault gouges (Imber *et al.* 2008; Lockner *et al.* 2011; Remitti *et al.* 2015), or because they are subjected to elevated pore fluid pressures (Sibson 2004).

6.3 Tectonic evolution of western New Guinea

Having constrained the present-day rheology and force balance in the New Guinea Highlands and their southern forelands, we now investigate the evolving force balance in western New Guinea. As described above, our analysis of normal-faulting earthquakes, GPS data, geomorphology, and seismic reflection profiles has shown that the Bird's Neck and Cenderawasih Bay are presently undergoing extension, but have been subjected to several stages of tectonic evolution throughout the Neogene and Quaternary (Figs 8, 9 and 10). The Lengguru Fold-Thrust Belt (LFTB) shows that the Bird's Neck has experienced significant crustal shortening, but has since been cut by more recent extensional faults observed both onshore within the LFTB and Wandamen Peninsula, and offshore in Cenderawasih Bay. Structural and sedimentological analysis suggests that the LFTB formed between 11 and 2 Ma (Bailly *et al.* 2009). This shortening may have been caused by the Weyland Overthrust: a rifted continental sliver which was thrust ∼25 km southwest over the Bird's Neck in the late Miocene, due to localized subduction in Cenderawasih Bay (Dow & Sukamto 1984; Hill & Hall 2003). François *et al.* (2016) analysed metamorphic assemblages from the Wandamen Peninsula and suggested that the rocks had been buried to 45 km depth at 8 Ma, followed by rapid exhumation around 5 Ma. Further metamorphic dating in the Wandamen Peninsula led White *et al.* (2019) to argue that formation of the LFTB was even younger, occurring between 5 and 3 Ma. Dating of the undeformed sediment layers observed in the western part of the seismic reflection profile, which blanket the fold-thrust belt, imply that shortening had ceased by 3.6 Ma (Fig. 10; Priastomo 2012). Most studies agree, however, that there was a shift to regional transtension approximately 2 Ma, which generated the cross-cutting normal faults seen in Fig. 9. This event was coeval with the generation of the Tarera-Aiduna Fault, and the initiation and reactivation of normal faults within the Paniai-Lowlands Fault Zone (Puntodewo *et al.* 1994; Stevens *et al.* 2002; Pubellier & Ego 2002; Bock *et al.* 2003; Bailly *et al.* 2009).

While this switch from tectonic compression to transtension in the early Pleistocene is generally accepted, it is uncertain what triggered this change in tectonic regime. Bailly *et al.* (2009) have previously attributed the cessation of shortening within the LFTB to slab rollback at the Seram Trench (Fig. 1b) and increasing friction during the development of the accretionary prism. They suggest that localized shortening within the LFTB, as a result of Australia–Pacific convergence, was transferred to the Seram Trench and adjacent accretionary prism after the formation of the Tarera-Aiduna Fault. However, this explanation does not explain the presence of normal-faulting roughly orthogonal to the previous shortening direction, and so other factors must also be involved. The other major tectonic change in the region at a similar time is the evolution of the Banda Arc. Spakman & Hall (2010) proposed that the extreme curvature of the Banda Arc has developed over the last ∼15 Myr as the Banda oceanic slab rolled back and the arc moved eastwards towards Australia and New Guinea. They suggest that the arc's curvature increased over time due to the subduction of a Jurassic oceanic embayment on the northwest margin of the Australian Plate, and the progressive folding of a single subducted slab at depth. We therefore investigate whether increasing curvature in the Banda Arc through time could have resulted in the change in tectonic style in western New Guinea around 2 Ma.

A summary of the tectonic evolution of western New Guinea is shown in Fig. 13, based on work by Pubellier & Ego (2002), Hill & Hall (2003), Bailly *et al.* (2009), Spakman & Hall (2010) and François *et al.* (2016). The development of increasing curvature in the Banda Arc will have increased the circumference of the Bird's Head Block, and thus also the magnitude of the plate driving forces exerted upon the block by the Banda Arc. We will here test whether this increase in force along the Banda Arc may have been responsible for the initiation of the Tarera-Aiduna Fault, reactivating faults in the Paniai-Lowlands Fault Zone, and changing the tectonic regime in the Bird's Neck and Cenderawasih Bay.

We have tested this hypothesis by performing simple force-balance calculations across the Bird's Head Block. In these calculations, we have chosen to model the Bird's Head Block as a rigid undeforming block, and to balance the forces acting upon it. This approach is motivated by there being negligible internal deformation within the BHB revealed by earthquakes (Fig. 4) or GPS (Fig. 8), and there being a series of long, rapidly slipping, fault zones on it's boundaries. In this case, balancing forces on a rigid

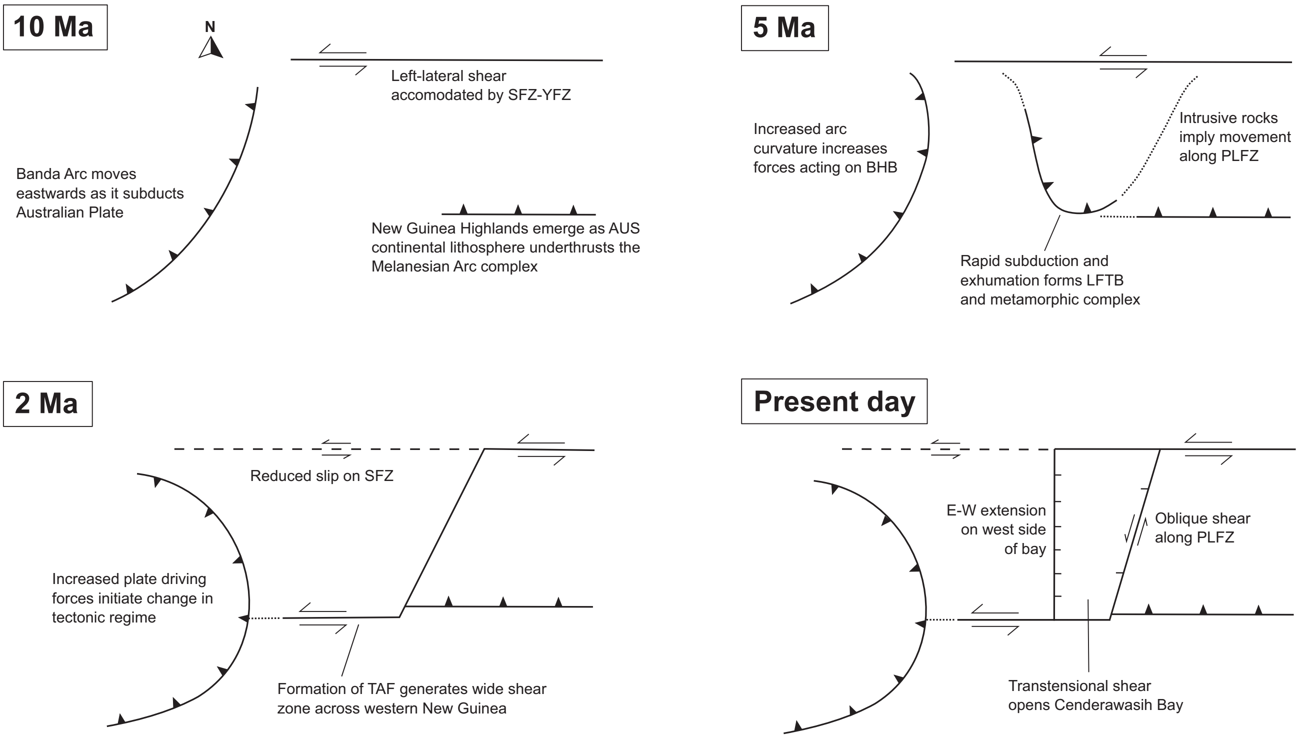

Figure 13. A simplified summary of the tectonic evolution of western New Guinea and the Banda Arc, showing the major fault zones and structures active over the past 10 My. BHB, Bird's Head Block; PLFZ, Paniai-Lowlands Fault Zone; SFZ-YFZ, Sorong/Yapen Fault Zone; TAF, Tarera-Aiduna Fault.

block is more appropriate than modelling the region as a continuum (England & McKenzie 1982). Because the topography strikes parallel to the fault zones bounding the block, any gravitational potential energy contrasts across these boundaries are included within the net forces on the boundaries that we investigate below. Additionally, provided that any basal drag on the base of the Bird's Head Block is parallel to the direction of motion on the subduction interface (i.e. that the mantle flow is controlled by the subducting slab), then this component of the force balance is also captured in the net force exerted by the Banda arc.

The main forces exerted upon the Bird's Head Block are caused by the major fault zones along its edges, namely the Banda Arc (subduction zone force) and the Sorong-Yapen Fault Zone in the north (shear zone force; Fig. 14a). By varying the forces exerted by these two major fault zones, and assuming that the net force exerted upon the Bird's Head Block is zero, we can resolve the forces to find the resultant force acting on the Bird's Neck and the eastern margin of Cenderawasih Bay (Fig. 14b). We can then compare this resultant force with the orientations of the fault zones and the slip vectors of earthquakes, to determine whether there is a combination of forces which may have been consistent with generating or reactivating the faults in this area, and creating the pattern of strike-slip and normal faulting observed today.

To calculate the possible net forces exerted on each boundary of the Bird's Head Block, we multiply the length of each fault zone along the block boundaries with a range of plausible values for the net force per unit length transmitted across the block boundaries. We use the present-day geometries of the fault zones to estimate the lengths, and assume that the fault zones have undergone insignificant geometric change over the past 2 Myr. The main uncertainty in these calculations is the force per unit length exerted across the block boundaries, and so we have varied this value over a wide range. To reflect the global uncertainty in the force balance in subduction zones (Forsyth & Uyeda 1975; Conrad & Hager 1999; Billen & Gurnis 2001; Conrad & Lithgow-Bertelloni 2004; Copley *et al.* 2010), and the additional complication of continental material thought to be entering the subduction zone at the Seram Trench (Stevens *et al.* 2002), we have varied the force per unit length exerted on the Bird's Head by the Banda Arc between 10 and -10×10^{12} N m^{-1}, where a positive value implies the force acts northeast and pushes the Bird's Head Block away from the Banda Arc, and a negative value implies the force acts southwest and pulls the BHB towards the subduction zone. For the Sorong-Yapen Fault Zone, we have modelled the shear force imparted onto the BHB by considering a shear stress between 1 and 30 MPa (similar to global earthquake stress drops; Allmann & Shearer 2009) acting over a fault depth of 0–30 km. This configuration generates a net shear force per unit length between 0.03 and 0.9×10^{12} N m^{-1} along-strike. As the SFZ-YFZ is left-lateral, the shear force acts westwards upon the Bird's Head Block.

Figs 14(c) and (d) show the azimuth and magnitude of the resultant force required to balance the forces exerted upon the Bird's Head Block, for each value of subduction zone and shear zone force per unit length. The azimuth represents the orientation of the force being exerted on the eastern margin of the Bird's Head Block by central New Guinea, so an east-directed azimuth represents extensional stress on the margin, and a north-directed azimuth represents left-lateral shear. The grey shading on Figs 14(c) and (d) shows the likely range of shear zone force per unit length, as discussed above. The purple shaded area shows the range of forces that are consistent with that shear zone force and also the required orientation of the resultant force given the orientation of left-lateral strike-slip and

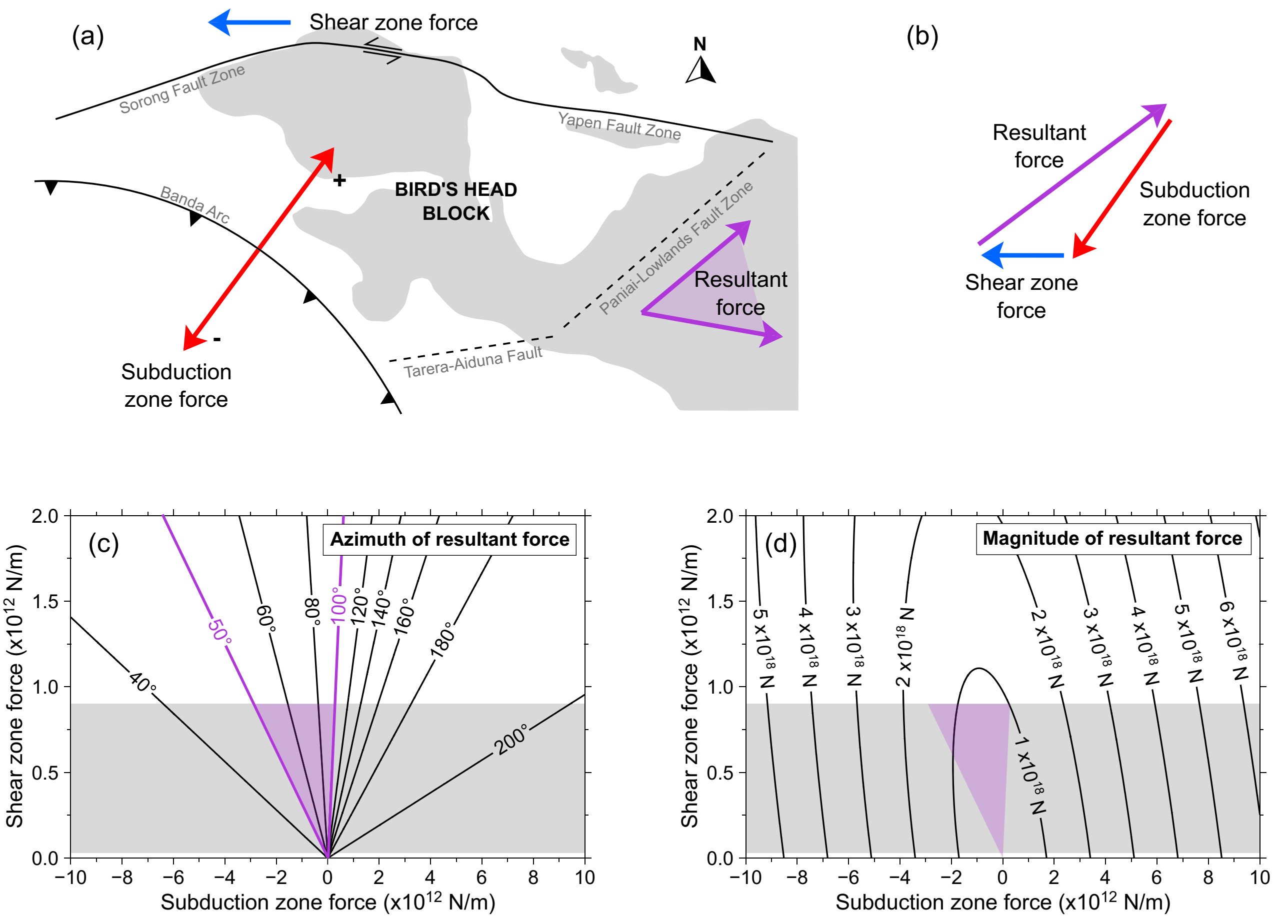

Figure 14. (a) Cartoon showing the major fault zones acting on the Bird's Head Block ~2 Ma, namely the Banda Arc and the Sorong and Yapen Fault Zones. The + and - symbols next to the subduction zone force indicate the designated positive and negative directions of the force acting from the Banda Arc onto the Bird's Head Block. The range of possible azimuths of the resultant force (purple shaded region) has been estimated from the slip vectors of earthquakes along the Tarera-Aiduna Fault and Paniai-Lowlands Fault Zone. (b) Vector summation of the subduction zone force from the Banda Arc and shear zone force from the Sorong and Yapen Fault Zones allows us to estimate the magnitude and azimuth of the resultant force acting on the Bird's Head Block. (c and d) Co-varying the magnitude of the subduction and shear zone forces (per metre along-strike) gives estimates of the magnitude and azimuth of the resultant force, plotted as contours. The grey shaded region indicates the plausible values of the shear zone force, and thus the most likely region of parameter space. Our estimate of the azimuth of the resultant force, determined from the slip vectors of recent earthquakes, is indicated by the purple shaded region.

normal-faulting earthquakes along the margins of Cenderawasih Bay (50–100°). This result shows that there is a plausible combination of forces from the Banda Arc and the Sorong-Yapen Fault Zone which could generate the observed faulting along the eastern margin of the Bird's Head Block, and thus the increased curvature of the Banda Arc may have been responsible for the present-day tectonic configuration of western New Guinea.

The magnitude of the resultant force ($<1.5 \times 10^{18}$ N), when averaged over a total fault length of ~600 km and a seismogenic thickness of 20 km, gives a stress estimate of <125 MPa (with no lower bound). Our results also show that the magnitude of the force exerted by the Banda Arc on the Bird's Head Block (subduction zone force) must be between –2.8 and 0.3×10^{12} N m^{-1}, with 50 per cent of the models between –2 and 0.2×10^{12} N m^{-1}. If the seismogenic thickness of the Sorong and Yapen Fault Zones is reduced from 30 to 20 km, the subduction zone force must be between –1.9 and 0.2×10^{12} N m^{-1}, with 50 per cent of the models between –1.3 and 0.1×10^{12} N m^{-1}. Negative values for this subduction zone force, acting as a 'slab pull' force on the Bird's Head Block, are consistent with the existence of the Aru Trough: a ~3.5 km deep depression located south of the Bird's Head, where GPS data and earthquake focal mechanisms show that the trough is actively extending (Jacobson *et al.* 1979; Bock *et al.* 2003; Sloan & Jackson 2012). Our estimates of the magnitude of the slab pull force from the Banda Arc (0–2.8×10^{12} N m^{-1}) are less than or equal to the values commonly inferred for other subduction zones (2–2.5×10^{12} N m^{-1}, Copley *et al.* 2010; 1–6×10^{12} N m^{-1}, Capitanio *et al.* 2009; 8–40×10^{12} N m^{-1}, Conrad & Lithgow-Bertelloni 2002 and Conrad & Lithgow-Bertelloni 2004). Our estimates may be lower than most previous estimates of the magnitude of 'slab pull' because of the effects of positively buoyant continental material impinging on the subduction zone.

7 CONCLUSIONS

We have combined new earthquake source parameters with thermal modelling, analysis of gravity anomalies and simple mechanical models in order to investigate the active and recent tectonics of New Guinea. We find that the pre-existing structural contrast across the Tasman Line in the Australian continental lithosphere plays an important role in controlling along-strike variations in the temperature structure, seismogenic thickness, and strength of the New Guinea foreland. These strength variations are reflected in the differing behaviour of the eastern foreland (where the crust appears broken through on high-angle faults) and the western foreland (where the crust appears mostly intact). Horizontal forces exerted between the New Guinea Highlands and forelands are estimated to be between 2–5 $\times$ 10^{12} N m^{-1} along-strike. From these results, we are able to constrain the effective coefficient of friction on crustal faults within the foreland basin to be 0.01–0.28. The lack of correlation between foreland seismogenic thickness and the elevation of the New Guinea Highlands is likely to represent the time taken for the growth of topography to mirror the spatially- and temporally-varying strength of the bounding foreland, as the thinned passive margin of the northern Australian continent is consumed. Recent changes in the configuration of faulting in western New Guinea imply a changing tectonic force balance on that region, which is likely to be due to the progressive development of curvature in the Banda Arc.

ACKNOWLEDGEMENTS

We thank Simon Lamb and Laura Webb for insightful and constructive reviews. We also thank Domenico Chiarella and Robert Hall for helping with access to literature at Royal Holloway University of London, James Jackson for useful comments on the manuscript, and Sam Wimpenny for assistance with coding. LK is supported by a Girdler Doctoral Scholarship. CB is supported by the Leverhulme grant 'Neptune' (RPG-2018-243).

DATA AVAILABILITY

We have used several freely available datasets for topographic, earthquake, and gravity data. ETOPO2 (2-minute gridded global relief) data were downloaded from the NOAA National Centers for Environmental Information web page (https://www.ngdc.noaa.gov/mgg/global/etopo2.html). SRTM30 (30-metre resolution global relief) data were downloaded from within the Generic Mapping Tools program (Wessel *et al.* 2019). Seismic waveforms were downloaded from the IRIS Data Management Centre (https://ds.iris.edu/wilber3). Additional earthquake source data were downloaded from the Global CMT catalogue (https://www.globalcmt.org; Dziewonski *et al.* 1981; Ekström *et al.* 2012) and the ISC-EHB Bulletin (http://www.isc.ac.uk/isc-ehb; Weston *et al.* 2018; International Seismological Centre 2021). GOCE free-air gravity anomalies were downloaded from the European Space Agency (https://earth.esa.int/eogateway/missions/goce). EIGEN-6C free-air gravity anomalies were downloaded from the International Centre for Global Earth Models (http://icgem.gfz-potsdam.de). All figures have been produced using Generic Mapping Tools v6 (Wessel *et al.* 2019) and Inkscape v0.92.3 (Project 2018).

REFERENCES

Abers, G. & McCaffrey, R., 1988. Active deformation in the New Guinea Fold-and-Thrust Belt: seismological evidence for strike-slip faulting and basement-involved thrusting, *J. geophys. Res.,* **93**(B11), 13 332–13 354.

Abers, G.A. & Lyon-Caen, H., 1990. Regional gravity anomalies, depth of the Foreland Basin and isostatic compensation of the New Guinea Highlands, *Tectonics,* **9**(6), 1479–1493.

Abers, G.A. & Roecker, S.W., 1991. Deep structure of an arc-continent collision: Earthquake relocation and inversion for upper mantle P and S wave velocities beneath Papua New Guinea, *J. geophys. Res.,* **96**(B4), 6379–6401.

Aitchison, J.C., Ireland, T.R., Blake, M.C.Jr & Flood, P.G., 1992. 530 Ma zircon age for ophiolite from the New England orogen: oldest rocks known from eastern Australia, *Geology,* **20**(2), 125.

Allmann, B.P. & Shearer, P.M., 2009. Global variations of stress drop for moderate to large earthquakes, *J. geophys. Res.,* **114**(B1), doi:10.1029/2008JB005821.

Artyushkov, E.V., 1973. Stresses in the lithosphere caused by crustal thickness inhomogeneities, *J. geophys. Res. (1896-1977),* **78**(32), 7675–7708.

Assumpção, M. & Suárez, G., 1988. Source mechanisms of moderate-size earthquakes and stress orientation in mid-plate South America, *J. geophys. Int.,* **92**(2), 253–267.

Babault, J., Viaplana-Muzas, M., Legrand, X., Van Den Driessche, J., González-Quijano, M. & Mudd, S.M., 2018. Source-to-sink constraints on tectonic and sedimentary evolution of the western Central Range and Cenderawasih Bay (Indonesia), *J. Asian Earth Sci.,* **156,** 265–287.

Bailly, V., Pubellier, M., Ringenbach, J.-C., de Sigoyer, J. & Sapin, F., 2009. Deformation zone 'jumps' in a young convergent setting; the Lengguru fold-and-thrust belt, New Guinea Island, *Lithos,* **113**(1–2), 306–317.

Baldwin, S.L., Fitzgerald, P.G. & Webb, L.E., 2012. Tectonics of the New Guinea Region, *Annu. Rev. Earth planet. Sci.,* **40**(1), 495–520.

Billen, M.I. & Gurnis, M., 2001. A low viscosity wedge in subduction zones, *Earth planet. Sci. Lett.,* **193**(1–2), 227–236.

Bock, Y., Prawirodirdjo, L., Genrich, J.F., Stevens, C.W., McCaffrey, R., Subarya, C., Puntodewo, S.S.O. & Calais, E., 2003. Crustal motion in Indonesia from Global Positioning System measurements, *J. geophys. Res.,* **108**(B8), doi:10.1029/2001JB000324.

Bollinger, L., Avouac, J.P., Cattin, R. & Pandey, M.R., 2004. Stress buildup in the Himalaya, *J. geophys. Res.,* **109**(B11), doi:10.1029/2003JB002911.

Bouhifd, M.A., Andrault, D., Fiquet, G. & Richet, P., 1996. Thermal expansion of forsterite up to the melting point, *Geophys. Res. Lett.,* **23**(10), 1143–1146.

Bourne, S.J., Árnadóttir, T., Beavan, J., Darby, D.J., England, P.C., Parsons, B., Walcott, R.I. & Wood, P.R., 1998. Crustal deformation of the Marlborough Fault Zone in the South Island of New Zealand: geodetic constraints over the interval 1982–1994, *J. geophys. Res.,* **103**(B12), 30 147–30 165.

Buchanan, P.G. & Warburton, J., 1996. The influence of pre-existing basin architecture in the development of the Papuan Fold and Thrust Belt: implications for petroleum prospective.

Burov, E. & Watts, A., 2006. The long-term strength of continental lithosphere: "jelly sandwich" or "crème brûlée"?, *GSA Today,* **16**(1), 4.

Burov, E.B., 2010. The equivalent elastic thickness (Te), seismicity and the long-term rheology of continental lithosphere: time to burn-out "crème brûlée"?: Insights from large-scale geodynamic modeling, *Tectonophysics,* **484**(1), 4–26.

Byerlee, J., 1978. Friction of Rocks, in *Rock Friction and Earthquake Prediction, Contributions to Current Research in Geophysics (CCRG),* pp. 615–626, eds Byerlee, J.D. & Wyss, M., Birkhäuser.

Capitanio, F.A., Morra, G. & Goes, S., 2009. Dynamics of plate bending at the trench and slab-plate coupling, *Geochem. Geophys. Geosyst.,* **10**(4), doi:10.1029/2008GC002348.

Cardwell, R.K. & Isacks, B.L., 1978. Geometry of the subducted lithosphere beneath the Banda Sea in eastern Indonesia from seismicity and fault plane solutions, *J. geophys. Res.,* **83**(B6), 2825–2838.

Carter, D.J., Audley-Charles, M.G. & Barber, A.J., 1976. Stratigraphical analysis of island arc—continental margin collision in eastern Indonesia, *J. geol. Soc.,* **132**(2), 179–198.

International Seismological Centre, 2021. ISC-EHB dataset, https://doi.org/10.31905/PY08W6S3.

Chapman, C.H., Jen-Yi, C., Lyness, D. & Doornbos, D., 1988. The WKBJ seismogram algorithm, in *Seismological Algorithms: Computational Methods and Computer Programs,* pp. 47–74, ed Doornbos, D.J., Academic Press.

Charlton, T., 1996. Correlation of the Salawati and Tomori Basins, eastern Indonesia: a constraint on left-lateral displacements of the Sorong fault zone, *Geol. Soc., Lond., Spec. Publ.,* **106,** 465–481.

Chen, W.-P. & Molnar, P., 1983. Focal depths of intracontinental and intraplate earthquakes and their implications for the thermal and mechanical properties of the lithosphere, *J. geophys. Res.,* **88**(B5), 4183–4214.

Chen, W.-P. & Molnar, P., 1990. Source parameters of earthquakes and intraplate deformation beneath the Shillong Plateau and the Northern Indoburman Ranges, *J. geophys. Res.,* **95**(B8), 12 527–12 552.

Clitheroe, G., Gudmundsson, O. & Kennett, B.L.N., 2000. The crustal thickness of Australia, *J. geophys. Res.,* **105**(B6), 13 697–13 713.

Cloos, M., Sapiie, B., Quarles van Ufford, A., Weiland, R.J., Warren, P.Q. & McMahon, T.P., 2005. *Collisional Delamination in New Guinea: The Geotectonics of Subducting Slab Breakoff,* Geological Society of America.

Coney, P.J., Edwards, A., Hine, R., Morrison, F. & Windrim, D., 1990. The regional tectonics of the Tasman orogenic system, eastern Australia, *J. Struct. Geol.,* **12**(5), 519–543.

Conrad, C.P. & Hager, B.H., 1999. Effects of plate bending and fault strength at subduction zones on plate dynamics, *J. geophys. Res.,* **104**(B8), 17 551–17 571.

Conrad, C.P. & Lithgow-Bertelloni, C., 2002. How mantle slabs drive plate tectonics, *Science,* **298**(5591), 207–209.

Conrad, C.P. & Lithgow-Bertelloni, C., 2004. The temporal evolution of plate driving forces: importance of "slab suction" versus "slab pull" during the Cenozoic, *J. geophys. Res.,* **109**(B10), doi:10.1029/2004JB002991.

Copley, A. & Woodcock, N., 2016. Estimates of fault strength from the Variscan foreland of the northern UK, *Earth planet. Sci. Lett.,* **451,** 108–113.

Copley, A., Boait, F., Hollingsworth, J., Jackson, J. & McKenzie, D., 2009. Subparallel thrust and normal faulting in Albania and the roles of gravitational potential energy and rheology contrasts in mountain belts, *J. geophys. Res.,* **114**(B5), doi:10.1029/2008JB005931.

Copley, A., Avouac, J.-P. & Royer, J.-Y., 2010. India-Asia collision and the Cenozoic slowdown of the Indian plate: implications for the forces driving plate motions, *J. geophys. Res.,* **115**(B3), doi:10.1029/2008JB005931.

Copley, A., Avouac, J.-P., Hollingsworth, J. & Leprince, S., 2011. The 2001 Mw 7.6 Bhuj earthquake, low fault friction, and the crustal support of plate driving forces in India, *J. geophys. Res.,* **116**(B8) doi:10.1029/2010JB008137.

Craig, T.J. & Jackson, J.A., 2021. Variations in the seismogenic thickness of East Africa, *J. geophys. Res.,* **126**(3), e2020JB020754, doi:10.1029/2020JB020754.

Craig, T.J., Jackson, J.A., Priestley, K. & McKenzie, D., 2011. Earthquake distribution patterns in Africa: their relationship to variations in lithospheric and geological structure, and their rheological implications: earthquake distribution patterns in Africa, *J. geophys. Int.,* **185**(1), 403–434.

Craig, T.J., Kelemen, P.B., Hacker, B.R. & Copley, A., 2020. Reconciling geophysical and petrological estimates of the thermal structure of Southern Tibet, *Geochem. Geophys. Geosyst.,* **21**(8), e2019GC008837, doi:10.1029/2019GC008837.

Crawford, A., Meffre, S. & Symonds, P., 2003. 120 to 0 Ma tectonic evolution of the Southwest Pacific and analogous geological evolution of the 600 to 220 Ma Tasman Fold Belt System, *Geol. Soc. Aust. Spec. Publ.,* **22,** 383–403.

Daczko, N.R., Caffi, P. & Mann, P., 2011. Structural evolution of the Dayman dome metamorphic core complex, eastern Papua New Guinea, *GSA Bull.,* **123**(11–12), 2335–2351.

Dalmayrac, B. & Molnar, P., 1981. Parallel thrust and normal faulting in Peru and constraints on the state of stress, *Earth planet. Sci. Lett.,* **55**(3), 473–481.

Davies, H.L., 2012. The geology of New Guinea - the cordilleran margin of the Australian continent, *Episodes,* **35**(1), 87–102.

Davies, H.L. & Jaques, A.L., 1984. Emplacement of ophiolite in Papua New Guinea, *Geol. Soc., Lond., Spec. Publ.,* **13**(1), 341–349.

Davies, H.L., Perembol, R.C.B., Winn, R.D. & KenGemar, P., 1997. *Terranes of the New Guinea Orogen,* p. 7.

Decker, J., Bergman, S., Teas, P. & Orange, D., 2009. Constraints on the tectonic evolution of the Bird's Head, West Papua, Indonesia, in *Indonesian Petroleum Association, 33rd Annual Convention and Exhibition,* Vol. **33,** doi:10.29118/IPA.556.09.G.139.

DeMets, C., Gordon, R.G., Argus, D.F. & Stein, S., 1994. Effect of recent revisions to the geomagnetic reversal time scale on estimates of current plate motions, *Geophys. Res. Lett.,* **21**(20), 2191–2194.

Devlin, S., Isacks, B.L., Pritchard, M.E., Barnhart, W.D. & Lohman, R.B., 2012. Depths and focal mechanisms of crustal earthquakes in the central Andes determined from teleseismic waveform analysis and InSAR, *Tectonics,* **31**(2), doi:10.1029/2011TC002914.

Dow, D. & Sukamto, R., 1984. Western Irian Jaya: The end-product of oblique plate convergence in the late tertiary, *Tectonophysics,* **106**(1–2), 109–139.

Drinkwater, M., Haagmans, R., Muzi, D., Popescu, A., Floberghagen, R., Kern, M. & Fehringer, M., 2007. The GOCE gravity mission: ESA's first core explorer, in *Proceedings of the 3rd International GOCE User Workshop,* 6–8 November 2006, ESA/ESRIN Frascati, Italy.

Dziewonski, A.M., Chou, T.-A. & Woodhouse, J.H., 1981. Determination of earthquake source parameters from waveform data for studies of global and regional seismicity, *J. geophys. Res.,* **86**(B4), 2825–2852.

Ekström, G., Nettles, M. & Dziewoński, A., 2012. The global CMT project 2004–2010: Centroid-moment tensors for 13,017 earthquakes, *Phys. Earth planet. Inter.,* **200–201,** 1–9.

Engdahl, E.R., van der Hilst, R. & Buland, R., 1998. Global teleseismic earthquake relocation with improved travel times and procedures for depth determination, *Bull. seism. Soc. Am.,* **88**(3), 722–743.

Engdahl, R.E., Jackson, J.A., Myers, S.C., Bergman, E.A. & Priestley, K., 2006. Relocation and assessment of seismicity in the Iran region, *J. geophys. Int.,* **167**(2), 761–778.

England, P. & Houseman, G., 1989. Extension during continental convergence, with application to the Tibetan Plateau, *J. geophys. Res.,* **94**(B12), 17 561–17 579.

England, P. & McKenzie, D., 1982. A thin viscous sheet model for continental deformation, *Geophys. J. R. astron. Soc.,* **70**(2), 295–321.

England, P. & Molnar, P., 2015. Rheology of the lithosphere beneath the central and western Tien Shan, *J. geophys. Res.,* **120**(5), 3803–3823.

England, P.C. & Houseman, G.A., 1988. The mechanics of the Tibetan Plateau, *Phil. Trans. R. Soc. Lond., A,* **326**(1589), 301–320.

Farr, T.G. *et al.*, 2007. The Shuttle Radar Topography Mission, *Rev. Geophys.,* **45**(2), doi:10.1029/2005RG000183.

Förste, C. *et al.*, 2014. EIGEN-6C4 - the latest combined global gravity field model including GOCE data up to degree and order 1949 of GFZ Potsdam and GRGS Toulouse, in *Proceedings of the EGU General Assembly Conference Abstracts,* Vol. **16,** pp. 3707.

Forsyth, D. & Uyeda, S., 1975. On the relative importance of the driving forces of plate motion, *J. geophys. Int.,* **43**(1), 163–200.

François, C., de Sigoyer, J., Pubellier, M., Bailly, V., Cocherie, A. & Ringenbach, J.-C., 2016. Short-lived subduction and exhumation in Western Papua (Wandamen peninsula): co-existence of HP and HT metamorphic rocks in a young geodynamic setting, *Lithos,* **266–267,** 44–63.

Gaina, C., Müller, R.D., Royer, J.-Y. & Symonds, P., 1999. Evolution of the Louisiade triple junction, *J. geophys. Res.,* **104**(B6), 12 927–12 939.

Glen, R.A., 2005. The Tasmanides of eastern Australia, *Geol. Soc., Lond., Spec. Publ.,* **246**(1), 23–96.

Granath, J., Soofi, K. & Mercer, J., 1991. Applications of SAR in structural modeling of the central ranges thrust belt, Irian Jaya, Indonesia, in *Proceedings of the Thematic Conference on Geologic Remote Sensing,* Denver, CO.

Haddad, D. & Watts, A.B., 1999. Subsidence history, gravity anomalies, and flexure of the northeast Australian margin in Papua New Guinea, *Tectonics,* **18**(5), 827–842.

Hall, R., 2002. Cenozoic geological and plate tectonic evolution of SE Asia and the SW Pacific: computer-based reconstructions, model and animations, *J. Asian Earth Sci.,* **20**(4), 353–431.

Hamilton, P.J., Johnson, R.W., Mackenzie, D.E. & O'Nions, R.K., 1983. Pleistocene volcanic rocks from the Fly-Highlands province of western Papua New Guinea: a note on new Sr and Nd isotopic data and their petrogenetic implications, *J. Volc. Geotherm. Res.,* **18**(1), 449–459.

Hamilton, W., 1979. *Tectonics of the Indonesian Region,* Vol. **1078,** US Government Printing Office.

Hasterok, D., Gard, M. & Webb, J., 2018. On the radiogenic heat production of metamorphic, igneous, and sedimentary rocks, *Geosci. Front.,* **9**(6), 1777–1794.

Herman, F. *et al.*, 2010. Exhumation, crustal deformation, and thermal structure of the Nepal Himalaya derived from the inversion of thermochronological and thermobarometric data and modeling of the topography, *J. geophys. Res.,* **115**(B6), doi:10.1029/2008JB006126.

Hill, K., 1991. Structure of the Papuan Fold Belt, Papua New Guinea, *AAPG Bull.,* **75**(5), 857–872.

Hill, K.C. & Hall, R., 2003. *Mesozoic-Cenozoic Evolution of Australia's New Guinea Margin in a West Pacific Context,* Geological Society of America.

Hill, K.C. & Raza, A., 1999. Arc-continent collision in Papua Guinea: constraints from fission track thermochronology, *Tectonics,* **18**(6), 950–966.

Hinschberger, F., Malod, J.-A., Réhault, J.-P., Villeneuve, M., Royer, J.-Y. & Burhanuddin, S., 2005. Late Cenozoic geodynamic evolution of eastern Indonesia, *Tectonophysics,* **404**(1), 91–118.

Hobson, D.M., 1986. A thin skinned model for the Papuan Thrust Belt and some implications for hydrocarbon exploration, *APPEA J.,* **26**(1), 214–225.

Hofmeister, A.M., 1999. Mantle values of thermal conductivity and the geotherm from phonon lifetimes, *Science,* **283**(5408), 1699–1706.

Imber, J., Holdsworth, R.E., Smith, S.A.F., Jefferies, S.P. & Collettini, C., 2008. Frictional-viscous flow, seismicity and the geology of weak faults: a review and future directions, *Geol. Soc., Lond., Spec. Publ.,* **299**(1), 151–173.

Jackson, J., McKenzie, D., Priestley, K. & Emmerson, B., 2008. New views on the structure and rheology of the lithosphere, *J. geol. Soc.,* **165**(2), 453–465.

Jackson, J., McKenzie, D. & Priestley, K., 2021. Relations between earthquake distributions, geological history, tectonics and rheology on the continents, *Phil. Trans. R. Soc. A.,* **379**(2193), 20190412.

Jackson, J.A. & White, N.J., 1989. Normal faulting in the upper continental crust: Observations from regions of active extension, *J. Struct. Geol.,* **11**(1), 15–36.

Jacobson, R.S., Shor, G.G.S.Jr, Kieckhefer, R.M. & Purdy, G.M., 1979. Seismic refraction and reflection studies in the Timor-Aru trough system and Australian continental shelf: convergent margins, in *AAPG MEMOIR: Geological and Geophysical Investigations of Continental Margins,* Vol. **29,** pp. 209–222, eds Watkins, J.S., Montadert, L. & Dickerson, P. W., American Association of Petroleum Geologists.

Jaupert, C., Labrosse, S., Lucazeau, F. & Mareschal, J.-C., 2015. Temperatures, heat, and energy in the mantle of the Earth, in *Treatise on Geophysics,* 2nd edn, Vol. **7,** pp. 223–270.

Johnson, R.W., Mackenzie, D.E. & Smith, I.E.M., 1978. Delayed partial melting of subduction-modified mantle in papua new guinea, *Tectonophysics,* **46**(1), 197–216.

Jost, B.M., Webb, M. & White, L.T., 2018. The Mesozoic and Palaeozoic granitoids of north-western New Guinea, *Lithos,* **312–313,** 223–243.

Karato, S.-I. & Wu, P., 1993. Rheology of the upper mantle: a synthesis, *Science,* **260**(5109), 771–778.

Kayal, J.R. & Zhao, D., 1998. Three-dimensional seismic structure beneath Shillong Plateau and Assam Valley, Northeast India, *Bull. seism. Soc. Am.,* **88**(3), 667–676.

Kennett, B.L.N., Engdahl, E.R. & Buland, R., 1995. Constraints on seismic velocities in the Earth from traveltimes, *J. geophys. Int.,* **122**(1), 108–124.

Kohlstedt, D.L., Evans, B. & Mackwell, S.J., 1995. Strength of the lithosphere: constraints imposed by laboratory experiments, *J. geophys. Res.,* **100**(B9), 17587–17602.

Koulali, A., Tregoning, P., McClusky, S., Stanaway, R., Wallace, L. & Lister, G., 2015. New Insights into the present-day kinematics of the central and western Papua New Guinea from GPS, *J. geophys. Int.,* **202**(2), 993–1004.

Kumar, A., Mitra, S. & Suresh, G., 2015. Seismotectonics of the eastern Himalayan and indo-burman plate boundary systems, *Tectonics,* **34**(11), 2279–2295.

Lamb, S., 2006. Shear stresses on megathrusts: implications for mountain building behind subduction zones, *J. geophys. Res.,* **111**(B7), doi:10.1029/2005JB003916.

Lamb, S., Moore, J.D.P., Perez-Gussinye, M. & Stern, T., 2020. Global whole lithosphere isostasy: implications for surface elevations, structure, strength, and densities of the continental lithosphere, *Geochem. Geophys. Geosyst.,* **21**(10), e2020GC009150, e2020GC009150 2020GC009150.

Lockner, D.A., Morrow, C., Moore, D. & Hickman, S., 2011. Low strength of deep San Andreas fault gouge from SAFOD core, *Nature,* **472**(7341), 82–85.

Lund, M.G., Austrheim, H. & Erambert, M., 2004. Earthquakes in the deep continental crust - insights from studies on exhumed high-pressure rocks, *J. geophys. Int.,* **158**(2), 569–576.

Mackwell, S.J., Zimmerman, M.E. & Kohlstedt, D.L., 1998. High-temperature deformation of dry diabase with application to tectonics on Venus, *J. geophys. Res.,* **103**(B1), 975–984.

Maggi, A., Jackson, J., McKenzie, D. & Priestley, K., 2000a. Earthquake focal depths, effective elastic thickness, and the strength of the continental lithosphere, *Geology,* **28**(6), 495–498.

Maggi, A., Jackson, J.A., Priestley, K. & Baker, C., 2000b. A re-assessment of focal depth distributions in southern Iran, the Tien Shan and northern India: do earthquakes really occur in the continental mantle?, *J. geophys. Int.,* **143**(3), 629–661.

McCaffrey, R., 1989. Seismological constraints and speculations on Banda arc tectonics, *Netherl. J. Sea Res.,* **24**(2), 141–152.

McCaffrey, R., 1996. Slip partitioning at convergent plate boundaries of SE Asia, *Geol. Soc., Lond., Spec. Publ.,* **106**(1), 3–18.

McCaffrey, R. & Abers, G., 1988. SYN3: a program for inversion of teleseismic body wave forms on microcomputers, Tech. rep., Defense Technical Information Center, Fort Belvoir, VA.

McCaffrey, R. & Abers, G.A., 1991. Orogeny in arc-continent collision: the Banda arc and western New Guinea, *Geology,* **19**(6), 563–566.

McCaffrey, R., Abers, G. & Zwick, P., 1991. Inversion of teleseismic body waves, *IASPEI Software library,* **3,** 81–166.

McDowell, F.W., McMahon, T.P., Warren, P.Q. & Cloos, M., 1996. Pliocene Cu-Au-bearing igneous intrusions of the Gunung Bijih (Ertsberg) District, Irian Jaya, Indonesia: K-Ar geochronology, *J. Geol.,* **104**(3), 327–340.

McKenzie, D. & Fairhead, D., 1997. Estimates of the effective elastic thickness of the continental lithosphere from Bouguer and free air gravity anomalies, *J. geophys. Res.,* **102**(B12), 27 523–27 552.

McKenzie, D., Jackson, J. & Priestley, K., 2005. Thermal structure of oceanic and continental lithosphere, *Earth planet. Sci. Lett.,* **233**(3), 337–349.

McKenzie, D., Yi, W. & Rummel, R., 2014. Estimates of Te from GOCE data, *Earth planet. Sci. Lett.,* **399,** 116–127.

McKenzie, D., Yi, W. & Rummel, R., 2015. Estimates of Te for continental regions using GOCE gravity, *Earth planet. Sci. Lett.,* **428,** 97–107.

Mei, S., Suzuki, A.M., Kohlstedt, D.L., Dixon, N.A. & Durham, W.B., 2010. Experimental constraints on the strength of the lithospheric mantle, *J. geophys. Res.,* **115**(B8), doi:10.1029/2009JB006873.

Miao, S.Q., Li, H.P. & Chen, G., 2014. Temperature dependence of thermal diffusivity, specific heat capacity, and thermal conductivity for several types of rocks, *J. Therm. Anal. Calorim*., **115**(2), 1057–1063.

Mitra, S., Priestley, K.F., Borah, K. & Gaur, V.K., 2018. Crustal structure and evolution of the eastern Himalayan Plate boundary system, northeast India, *J. geophys. Res.,* **123**(1), 621–640.

Molnar, P. & Lyon-Caen, H., 1988. Some simple physical aspects of the support, structure, and evolution of mountain belts, in *Processes in Continental Lithospheric Deformation,* Vol. **218,** pp. 179–207, Clark Jr., S.P., Burchfiel, B.C. & Suppe, J., Geological Society of America.

Molnar, P. & Lyon-Caen, H., 1989. Fault plane solutions of earthquakes and active tectonics of the Tibetan Plateau and its margins, *J. geophys. Int.,* **99**(1), 123–154.

Moore, C., 2003. *New Guinea: Crossing Boundaries and History,* University of Hawaii Press.

Nash, C.R., Artmont, G., Gillan, M.L., Lennie, D., O'Connor, G. & Parris, K.R., 1993. Structure of the Irian Jaya Mobile Belt, Irian Jaya, Indonesia, *Tectonics,* **12**(2), 519–535.

Nemati, M., Hollingsworth, J., Zhan, Z., Bolourchi, M.J. & Talebian, M., 2013. Microseismicity and seismotectonics of the South Caspian Lowlands, NE Iran, *J. geophys. Int.,* **193**(3), 1053–1070.

Nissen, E., Tatar, M., Jackson, J.A. & Allen, M.B., 2011. New views on earthquake faulting in the Zagros fold-and-thrust belt of Iran: earthquake faulting in the Zagros, *J. geophys. Int.,* **186**(3), 928–944.

Pérez-Gussinyé, M., Lowry, A.R. & Watts, A.B., 2007. Effective elastic thickness of South America and its implications for intracontinental deformation, *Geochem. Geophys. Geosyst.,* **8**(5), doi:10.1029/2006GC001511.

Pieters, P.E., Pigram, C.J., Trail, D.S., Dow, D.B., Ratman, N. & Sukamto, R., 1983. The stratigraphy of western Irian Jaya, in *Proceedings of the of the 12th Indonesian Petroleum Association's Annual Convention and Exhibition,* pp. 229–261.

Pigram, C. & Symonds, P., 1991. A review of the timing of the major tectonic events in the New Guinea Orogen, *J. Southeast Asian Earth Sci.,* **6**(3–4), 307–318.

Pigram, C.J. & Panggabean, H., 1984. Rifting of the northern margin of the Australian continent and the origin of some microcontinents in Eastern Indonesia, *Tectonophysics,* **107**(3), 331–353.

Pigram, C.J., Davies, P.J., Feary, D.A. & Symonds, P.A., 1989. Tectonic controls on carbonate platform evolution in southern Papua New Guinea: passive margin to foreland basin, *Geology,* **17**(3), 199–202.

Plumb, K.A., 1979. The tectonic evolution of Australia, *Earth-Sci. Rev.,* **14**(3), 205–249.

Press, W., Teukolsky, S., Vetterling, W. & Flannery, B., 1992. *Numerical Recipes: The Art of Scientific Computing,* 2nd end, Cambridge Univ. Press.

Priastomo, Y.S., 2012. Tectonostratigraphy evolution of Cendrawasih Bay Basin Papua, Indonesia, *MSc thesis*, Royal Holloway University of London, London.

Priestley, K., Jackson, J. & McKenzie, D., 2008. Lithospheric structure and deep earthquakes beneath India, the Himalaya and southern Tibet, *J. geophys. Int.,* **172**(1), 345–362.

Priestley, K., McKenzie, D. & Ho, T., 2018. A lithosphere–asthenosphere boundary—a global model derived from multimode surface-wave tomography and petrology, in *Lithospheric Discontinuities,* pp. 111–123, American Geophysical Union.

Project, I., 2018. Inkscape v0.92.3., Inkscape v0.92.3. https://inkscape.org.

Pubellier, M. & Ego, F., 2002. Anatomy of an escape tectonic zone: Western Irian Jaya (Indonesia), *Tectonics,* **21**(4), 1–1-1-16.

Puntodewo, S. *et al.*, 1994. GPS measurements of crustal deformation within the Pacific-Australia plate boundary zone in Irian Jaya, Indonesia, *Tectonophysics,* **237**(3–4), 141–153.

Remitti, F., Smith, S.A.F., Mittempergher, S., Gualtieri, A.F. & Toro, G.D., 2015. Frictional properties of fault zone gouges from the J-FAST drilling project (Mw 9.0 2011 Tohoku-Oki earthquake), *Geophys. Res. Lett.,* **42**(8), 2691–2699.

Royer, J.-Y. & Sandwell, D.T., 1989. Evolution of the eastern Indian Ocean since the Late Cretaceous: Constraints from Geosat altimetry, *J. geophys. Res.: Solid Earth,* **94**(B10), 13755–13782.

Rudnick, R. & Nyblade, A., 1999. The thickness and heat production of Archean lithosphere, constraints from xenolith thermobarometry and surface heat flow, in *Mantle Petrology: Field Observations and High Pressure Experimentation: A Tribute to Francis R. (Joe) Boyd*, Special Publication No. 6, pp. 3–12, eds Fei Y., Bertka C.M., Mysen B.O., The Geochemical Society.

Rudnick, R.L., McDonough, W.F. & O'Connell, R.J., 1998. Thermal structure, thickness and composition of continental lithosphere, *Chem. Geol.,* **145**(3–4), 395–411.

Sapiie, B., Adyagharini, A.C. & Teas, P., 2010. New insight of tectonic evolution of Cendrawasih Bay and its implications for hydrocarbon prospect, Papua, Indonesia, in *Proceedings of the of the 34th Indonesian Petroleum Association's Annual Convention and Exhibition,* Indonesian Petroleum Association.

Schiebner, E., 1974. Fossil fracture zones (transform faults), segmentation and correlation problems in the Tasman Fold Belt System, in *Proceedings of the Tasman Geosyncline– A Symposium in Honour of Professor Dorothy Hill,* Queensland Division Geological Society of Australia, Brisbane, pp. 65–96.

Scholz, C.H., 1982. Scaling laws for large earthquakes: consequences for physical models, *Bull. seism. Soc. Am.,* **72**(1), 1–14.

Scholz, C.H. & Contreras, J.C., 1998. Mechanics of continental rift architecture, *Geology,* **26**(11), 967–970.

Sibson, R.H., 2004. Controls on maximum fluid overpressure defining conditions for mesozonal mineralisation, *J. Struct. Geol.,* **26**(6), 1127–1136.

Siebert, L., Simkin, T. & Kimberly, P., 2011. *Volcanoes of the World,* Univ. California Press.

Sloan, R.A. & Jackson, J.A., 2012. Upper-mantle earthquakes beneath the Arafura Sea and south Aru Trough: implications for continental rheology, *J. geophys. Res.,* **117**(B5), doi:10.1029/2011JB008992.

Sloan, R.A., Jackson, J.A., McKenzie, D. & Priestley, K., 2011. Earthquake depth distributions in central Asia, and their relations with lithosphere thickness, shortening and extension: earthquake depth distributions in central Asia, *J. geophys. Int.,* **185**(1), 1–29.

Spakman, W. & Hall, R., 2010. Surface deformation and slab– mantle interaction during Banda arc subduction rollback, *Nat. Geosci.,* **3**(8), 562–566.

Stevens, C.W., Mccaffrey, R., Bock, Y., Genrich, J.F., Pubellier, M. & Subarya, C., 2002. Evidence for block rotations and Basal shear in the World's fastest slipping continental shear zone in NW New Guinea, in *Geodynamics Series,* pp. 87–99, eds Stein, S. & Freymueller, J.T., American Geophysical Union.

Taymaz, T., Jackson, J. & Westaway, R., 1990. Earthquake mechanisms in the Hellenic Trench near Crete, *J. geophys. Int.,* **102**(3), 695–731.

Teas, P.A., Decker, J., Orange, D. & Baillie, P., 2009. New insight into structure and tectonics of the seram trough from SeaSeep^{TM} high resolution bathymetry, in *Proceedings of the 33rd Indonesian Petroleum Association Annual Exhibition & Convention*.

Townend, J. & Zoback, M.D., 2000. How faulting keeps the crust strong, **28**(5), 399–402.

Tregoning, P. & Gorbatov, A., 2004. Evidence for active subduction at the New Guinea Trench, *Geophys. Res. Lett.,* **31**(13), doi:10.1029/2004GL020190.

Turcotte, D.L. & Schubert, G., 2002. *Geodynamics,* Cambridge Univ. Press.

Veevers, J., Powell, C. & Roots, S., 1991. Review of seafloor spreading around Australia. I. Synthesis of the patterns of spreading, *Aust. J. Earth Sci.,* **38**(4), 373–389.

Veevers, J.J., 2000. *Billion-Year Earth History of Australia and Neighbours in Gondwanaland,* GEMOC Press.

Visser, W. & Hermes, J., 1962. Geological results of the exploration for oil in Netherlands New Guinea, Government Printing Office, The Hague, pp. 256.

Wallace, L.M. *et al.*, 2004. GPS and seismological constraints on active tectonics and arc-continent collision in Papua New Guinea: Implications for mechanics of microplate rotations in a plate boundary zone, *J. geophys. Res.,* **109**(B5), doi:10.1029/2003JB002481.

Webb, L.E., Baldwin, S.L. & Fitzgerald, P.G., 2014. The Early-Middle Miocene subduction complex of the Louisiade Archipelago, southern margin of the Woodlark Rift, *Geochem. Geophys. Geosyst.,* **15**(10), 4024–4046.

Weissel, J.K. & Watts, A.B., 1979. Tectonic evolution of the Coral Sea Basin, *J. geophys. Res.,* **84**(B9), 4572–4582.

Weller, O.M., Jackson, S., Miller, W. G.R., St-Onge, M.R. & Rayner, N., 2020. Quantitative elemental mapping of granulite-facies monazite: textural insights and implications for petrochronology, *J. Metamor. Geol.,* **38**(8), 853–880.

Wessel, P., Luis, J.F., Uieda, L., Scharroo, R., Wobbe, F., Smith, W.H.F. & Tian, D., 2019. The generic mapping tools version 6, *Geochem. Geophys. Geosyst.,* **20**(11), 5556–5564.

Weston, J., Engdahl, E.R., Harris, J., Di Giacomo, D. & Storchak, D.A., 2018. ISC-EHB: reconstruction of a robust earthquake data set, *Geophys. J. Int.,* **214**(1), 474–484.

White, L.T., Hall, R., Gunawan, I. & Kohn, B., 2019. Tectonic mode switches recorded at the northern edge of the Australian Plate during the Pliocene and Pleistocene, *Tectonics,* **38**(1), 281–306.

Whittington, A.G., Hofmeister, A.M. & Nabelek, P.I., 2009. Temperature-dependent thermal diffusivity of the Earth's crust and implications for magmatism, *Nature,* **458**(7236), 319–321.
Wimpenny, S., Copley, A., Benavente, C. & Aguirre, E., 2018. Extension and dynamics of the andes inferred from the 2016 Parina (Huarichancara) Earthquake, *J. geophys. Res.,* **123**(9), 8198–8228.
Yakymchuk, C. & Brown, M., 2019. Divergent behaviour of Th and U during anatexis: implications for the thermal evolution of orogenic crust, *J. Metamor. Geol.,* **37**(7), 899–916.
Zwick, P., McCaffrey, R. & Abers, G., 1994. MT5 Program, *IASPEI Software Library*. 4.

SUPPORTING INFORMATION

Supplementary data are available at *GJI* online.

Figure S1. Minimum misfit solution for the earthquake on 25 May 1992.
Figure S2. Minimum misfit solution for the earthquake on 12 June 1993.
Figure S3. Minimum misfit solution for the earthquake on 4 January 1994.
Figure S4. Minimum misfit solution for the earthquake on 13 March 1995.
Figure S5. Minimum misfit solution for the earthquake on 3 March 2000.
Figure S6. Minimum misfit solution for the earthquake on 2 February 2005. Due to the poor azimuthal distribution of stations, the gCMT focal mechanism solution was retained and we inverted only for centroid depth, magnitude and source time function.
Figure S7. Minimum misfit solution for the earthquake on 20 August 2007.
Figure S8. Minimum misfit solution for the earthquake on 15 November 2011.
Figure S9. Minimum misfit solution for the earthquake on 12 October 2012.
Figure S10. Minimum misfit solution for the earthquake on 8 December 2012.
Figure S11. Minimum misfit solution for the earthquake on 5 September 2013. Due to the poor azimuthal distribution of stations, the gCMT focal mechanism solution was retained and we inverted only for centroid depth, magnitude and source time function.
Figure S12. Minimum misfit solution for the earthquake on 28 July 2014.
Figure S13. Minimum misfit solution for the earthquake on 6 March 2018.
Figure S14. Minimum misfit solution for the earthquake on 26 January 2019.
Figure S15. Best-fitting solution for the earthquake on 23 February 1991.
Figure S16. Best-fitting solution for the earthquake on 21 January 1995.
Figure S17. Best-fitting solution for the earthquake on 25 October 1999.
Figure S18. Best-fitting solution for the earthquake on 12 July 2001.
Figure S19. Best-fitting solution for the earthquake on 28 September 2002.
Figure S20. Best-fitting solution for the earthquake on 19 August 2007.
Figure S21. Best-fitting solution for the earthquake on 29 October 2009.
Figure S22. Best-fitting solution for the earthquake on 14 June 2016.
Figure S23. Best-fitting solution for the earthquake on 27 April 2019.
Figure S24. Depth to the 350 °C isotherm plotted as a function of lithosphere thickness and radiogenic heating in the crust. There is no parameter space over which the depth to the 350 °C isotherm is greater than or equal to the seismogenic thickness in the foreland, for the appropriate values of lithosphere thickness (blue and pink bars marked 'West' and 'East'; Priestley *et al.* 2008).
Figure S25. (a) EIGEN-6C free-air gravity map of New Guinea (Förste *et al*. 2014). The green and purple coloured boxes represent the region over which profiles through the gravity field, perpendicular to the range front, have been stacked along the length of the west and east foreland basin, respectively. The coloured circles represent nodes which have been placed over the gravity minimum. (b and c) Mean (solid black line) and standard deviation bounds (dashed black lines) for the stacked GOCE free-air gravity anomalies, and the best-fitting flexural model to the observed gravity profile (solid coloured line). (d) Weighted misfit between the observed and modelled gravity field, plotted as a function of elastic thickness of the underthrusting Australian Plate. The best-fitting solutions for the west and east occur at $T_e = 4.6$ km and $T_e = 6.2$ km, respectively.

Please note: Oxford University Press is not responsible for the content or functionality of any supporting materials supplied by the authors. Any queries (other than missing material) should be directed to the corresponding author for the paper.